An inversion method for cometary atmospheres

B. Hubert[(a)], C. Opitom[(a)], D. Hutsemékers[(a)], E. Jehin[(a)], G. Munhoven[(a)], J. Manfroid[(a)], D.V. Bisikalo[(b)], V.I. Shematovich[(b)]

a. Institute of Astrophysics and Geophysics of the University of Liège, Liège, Belgium
Postal address: Allée du Six-Août, 19C, B-4000 Liège, BELGIUM.

b. Institute of Astronomy of the Russian Academy of Sciences, Moscow, Russia
Postal address: Pyatnitskaya street, 48, 119017 Moscow, RUSSIA.

Please cite this article as:
B. Hubert , C. Opitom , D. Hutsemekers , E. Jehin, G. Munhoven, J. Manfroid, D.V. Bisikalo, V.I. Shematovich, An inversion method for cometary atmospheres, Icarus (2016), doi: 10.1016/j.icarus.2016.04.044

Corresponding author:
B. Hubert (b.hubert@ulg.ac.be)

Keywords:
Comets; Comets, coma; Data reduction techniques

Submitted to Icarus
November 2015.
Revised January 2016

Abstract

Remote observation of cometary atmospheres produces a measurement of the cometary emissions integrated along the line of sight. This integration is the so-called Abel transform of the local emission rate. The observation is generally interpreted under the hypothesis of spherical symmetry of the coma. Under that hypothesis, the Abel transform can be inverted. We derive a numerical inversion method adapted to cometary atmospheres using both analytical results and least squares fitting techniques. This method, derived under the usual hypothesis of spherical symmetry, allows us to retrieve the radial distribution of the emission rate of any unabsorbed emission, which is the fundamental, physically meaningful quantity governing the observation. A Tikhonov regularization technique is also applied to reduce the possibly deleterious effects of the noise present in the observation and to warrant that the problem remains well posed. Standard error propagation techniques are included in order to estimate the uncertainties affecting the retrieved emission rate. Several theoretical tests of the inversion techniques are carried out to show its validity and robustness. In particular, we show that the Abel inversion of real data is only weakly sensitive to an offset applied to the input flux, which implies that the method, applied to the study of a cometary atmosphere, is only weakly dependent on uncertainties on the sky background which has to be subtracted from the raw observations of the coma. We apply the method to observations of three different comets observed using the TRAPPIST telescope: 103P/ Hartley 2, F6/ Lemmon and A1/ Siding Spring. We show that the method retrieves realistic emission rates, and that characteristic lengths and production rates can be derived from the emission rate for both CN and C_2 molecules. We show that the retrieved characteristic lengths can differ from those obtained from a direct least squares fitting over the observed flux of radiation, and that discrepancies can be reconciled for by correcting this flux by an offset (to which the inverse Abel transform is nearly not sensitive). The A1/Siding Spring observations were obtained very shortly after the comet produced an outburst, and we show that the emission rate derived from the observed flux of CN emission at 387 nm and from the C_2 emission at 514.1 nm both present an easily-identifiable shoulder that corresponds to the separation between pre- and post-outburst gas. As a general result, we show that diagnosing properties and features of the coma using the emission rate is easier than directly using the observed flux, because the Abel transform produces a smoothing that blurs the signatures left by features present in the coma. We also determine the parameters of a Haser model fitting the inverted data and fitting the line-of-sight integrated observation, for which we provide the exact analytical expression of the line-of-sight integration of the Haser model.

1. INTRODUCTION

Comets are relatively small size bodies formed at the early stages of the solar system evolution some 4.6 billions of years ago. They are often considered as potential tracers of conditions prevailing at that time (Ehrenfreund & Charnley, 2000). They mainly consist of an icy water nucleus with other constituents such as carbon monoxide (CO), carbon dioxide (CO_2), and dust. When these bodies escape their reservoirs, mainly the Oort cloud and the Kuiper belt, and approach the sun, they slowly warm up under the effect of solar radiation and their ices start to sublimate, releasing water vapor, CO, CO_2, dust and other minor species. This process produces a large, highly rarefied, expanding atmosphere: the coma, surrounding the icy nucleus.

The coma is exposed to the sun radiation and in particular to the ultraviolet solar flux, which is capable to trigger photochemical processes such as dissociation and ionization of the gaseous material. Many previous studies focused on the complex photochemistry of the coma from a theoretical and observational standpoint. Among others, Bhardwaj & Raghuram (2012) developed a photochemical model of the coma of comet C/1996 B2 (Hyakutake) to analyze the metastable oxygen $O(^1D)$ and $O(^1S)$ populations and emissions accounting for photodissociation and electron impact dissociation of H_2O, OH, CO and CO_2, as well as the dissociative recombination of ions H_2O^+, OH^+, CO^+ and CO_2^+ and direct electron impact on oxygen atoms. Loss mechanisms of metastable oxygen were the radiative decay, quenching and reaction with H_2O, CO and CO_2. The densities of the major species of the coma (H_2O, CO, CO_2 and OH) were given by a Haser model (Biver et al., 1999). Bhardwaj & Raghuram (2012) conducted an analysis aimed at matching the observed and computed ratio of the 557.7 nm green emission of $O(^1S)$ to the 630.0 and 636.4 nm red emissions of $O(^1D)$, from which they derived the CO_2 abundance and several photochemical parameters. Raghuram & Bhardwaj (2012) also applied the same model with adapted parameters to comet C/1995 Hale Bopp. Bisikalo et al. (2015) developed a model of the photochemistry of $O(^1D)$ and $O(^1S)$ using a Monte Carlo method to solve the Boltzmann equation to retrieve the energy distribution of these species across the expanding coma. They showed that the exothermic nature of the photochemical mechanisms producing metastable oxygen yields a strongly non-thermal distribution of their kinetic energy, which in turn produces a strongly non-gaussian emission line profile.

The radial distribution of cometary constituents if often described using a Haser model (Haser, 1957). This model is used for its simplicity and its ability to describe a spherically symmetric expanding coma. It relies on flux conservation and includes the effect of photochemical production and loss of any species in an ad hoc manner, instead of solving for the detailed photochemistry. Simple flux conservation produces a radial profile that varies as $1/r^2$, with r the radial distance:

$$n = \frac{Q}{4\pi r^2\, v} \tag{1}$$

with n the density of the species considered (H_2O, for example), Q the rate at which the comet's nucleus releases that species, and v the radial outflow speed of the emitting particles.

The concentration of a species that gets destroyed by photochemical processes decays exponentially with time, with a life time τ_p. This life time depends on solar activity, heliocentric distance etc. and translates into a characteristic length L_p in the expanding coma, so that the density profile becomes:

$$n_p = \frac{Q_p}{4\pi r^2\, v_p} e^{-\frac{r}{L_p}} \tag{2}$$

Here, the subscript p stands for "parent", as we are considering molecules outgassed by the comet's nucleus that decompose and produce "daughter" species, and which will be denoted by subscript d. The production rate of the daughter species is determined by the loss rate of their parent molecules. Daughter species can in turn be destroyed by photochemical processes, with a characteristic length L_d. Their density profile in the expanding atmosphere is then given by

$$n_d = \frac{Q_p}{4\pi r^2\, v_d} \frac{L_d}{L_d - L_p} \left(e^{-\frac{r}{L_d}} - e^{-\frac{r}{L_p}} \right). \tag{3}$$

The model could even be further complexified to derive the density profile of grand-daughter species. Expression (1) is however not integrable over $\mathbb{R}^3$ (accounting for the Jacobian of spherical coordinates) as $r \rightarrow \infty$, which clearly shows equation (1) does not suffice. The Haser model also assumes the characteristic length does not vary across the coma and that there exist only one production and one loss mechanism of the daughter species, which is not warrantied. As the daughter molecules are produced isotropically in a frame of reference moving with the expanding gas, there is no reason to assume that the expansion velocity of the different species can largely differ, and a single expansion velocity is generally used. However, the Haser model neglects molecular diffusion that can influence the density distribution. Integration of expressions (2) and (3) (multiplied by the appropriate Jacobian) over $\mathbb{R}^3$ can be easily carried out analytically, giving $Q_p\, L_d/v_d$ for the total content of daughter species particles of the coma. Models of the coma, either idealized using the Haser approximation or based upon a mechanistic representation such as those of Bhardwaj and Raghuram (2012), Bisikalo et al. (2015), Combi (1996), Rubin et al. (2011), Weiler (2007, 2012), Combi and Fink (1997) and others have to be compared against observational data. However, the local densities, which are the natural outputs of the models, cannot be directly observed remotely, as we discuss in the next section. Moreover, comets are dynamic objects, and time variations of the activity translate to radial gradients in the density, that are not accounted for by steady-state models, whatever their degree of sophistication. This is particularly significant when a comet produces an outburst.

Here, we present a method to retrieve the local emission rate from remote sensing observations of cometary atmospheres. Remote sensing of cometary emission provides only a line-of-sight integration of the emission rate, also called its Abel transform. We develop a method that inverts the Abel transform in the special case of cometary atmospheres. Section 2 presents the mathematical developments on which the inverse Abel transform relies. The result of this inversion must not be confused with a model of the coma. It is rather a direct processing of the observational data. Fundamentally, the result of the inverse Abel transform of the data contains essentially the same information as the initial line-of-sight integrated radial profile. In section 3, we present results from numerical tests that were done to validate the inversion method and highlight its benefits. In section 4, we present the results from applications of our inverse Abel transform method for three comets. These results are compared with Haser model fits to the data. Particular attention will be given to an outburst case. In section 5 we discuss the reach of the results obtained with the inverse Abel transform. We conclude with a short summary of our results in section 6. Appendix 1 provides additional analytical results that allow for a further refinement of the inversion method. These results do not appear to offer a crucial improvement in the case of cometary atmospheres but they could nevertheless prove useful for planetary atmospheres. Finally, appendix 2 gives the results needed to perform the exact analytical computation of the Abel transform of a cometocentric profile described using a Haser model,which is a result that can be used for any study dedicated to the analysis of observations of comets under the Haser hypothesis.

2. THE ABEL TRANSFORM INVERSION

A distant observer looking at the coma of a comet has no direct access to the density profile of the constituents. Excited species relax by emitting photons and the observation sums up the emission rates along a full line of sight according to the geometry described in **Figure 1**. If we denote by $n(r)$ the density of an excited atom or molecule (for example) and by A_{ul} the Einstein transition parameter for spontaneous emission of this excited particle by a transition from upper state u to lower state l, the emission rate at that radius is given by $f(r) = A_{ul}\, n(r)$. In principle, the local density can thus be immediately obtained, if the local emission rate profile is known. When molecular bands are observed and their spectral structure remains unresolved (which is generally the case), the characterization of the excited molecule density based on the emission rate may require a more sophisticated treatment. The fundamental principle remains nevertheless unchanged: it is possible to relate emission rates to molecular densities. In the geometrical framework of **Figure 1**, the line-of-sight integrated emission can be written:

$$F(r_0) = \int_{-\infty}^{+\infty} ds\, f(s) = 2\int_{0}^{+\infty} ds\, f(s) = 2\int_{r_0}^{+\infty} dr\, \frac{r}{\sqrt{r^2 - r_0^2}}\, f(r) \tag{4}$$

where r_0 is the tangent radius, i.e., the distance between the comet's center and the point of the line of sight closest to this center, f is the quantity to be integrated along the line of sight, such as the emission rate of a given excited species, or any other quantity. The coma is supposed to have a spherical symmetry (which allows us to change the integral over s from $-\infty$ to $+\infty$ to the double of the integral from 0 to $+\infty$ and to apply the variable change $s = \sqrt{r^2 - r_0^2}$, which has a jacobian $J = r/\sqrt{r^2 - r_0^2}$. The right-hand side of equation (4) is called the Abel transform of $f(r)$ (Bracewell, 1999). It has a well-known inverse transform:

$$f(r) = \frac{-1}{\pi}\int_{r}^{\infty} dr_0\, \frac{1}{\sqrt{r_0^2 - r^2}}\, \frac{dF(r_0)}{dr_0} \tag{5}$$

This expression is, however, of little practical usage, as it requires the computation of the derivative of $F(r_0)$, a difficult task especially when values for F are actually only available from a limited, discrete set of noisy data. Numerical inversion methods have thus been derived that use least squares fitting techniques and simple analytical expressions of the direct Abel transform, that can be obtained when $f(r) = r^n$, for $n \geq -1$. Indeed, let us denote by $I_n(r, r_0)$ the indefinite integral

$$I_n = \int dr \, \frac{r}{\sqrt{r^2 - r_0^2}} \, r^n. \tag{6}$$

An integration by parts shows that the I_n satisfy a simple recurrence relation:

$$\begin{aligned} &(n+1)I_n + n\, r_0^2 \, I_{n-2} = r^n \sqrt{r^2 - r_0^2} \\ &I_{-1} = \text{arcosh}\left(\frac{r}{r_0}\right) = ln\left(\frac{r}{r_0} + \sqrt{\frac{r^2}{r_0^2} - 1}\right) \\ &I_0 = \sqrt{r^2 - r_0^2} \end{aligned} \tag{7}$$

I_{-1} and I_0 can be directly obtained from equation (6). Although the recurrence relation (7) is formally of order 2, it can actually be solved as two joint first order linear recurrences, one for $n = 2m$ and one for $n = 2m + 1$, starting from I_0 and I_{-1}, respectively. Each I_n is defined up to an additive constant, which we can take as 0 because we will only use the results to compute definite integrals (so that the constants cancel out). These results have been used to derive numerical inversion techniques by several authors to study the emissions of planetary atmospheres (e.g., Quémerais et al., 2006, Stiepen et al., 2012; Cox et al., 2008) using the following ideas.

Any observation of the line of sight-integrated emission (i.e., brightness) of a given atmospheric emission will produce a discretized, noisy profile of values obtained for a series of tangent radii. Such profiles are generally called vertical profiles in the case of a planetary atmosphere or nucleo-centric profiles in the case of a coma. It then becomes natural to represent the emission rate profile $f(r)$ as a set of linear segments across well-chosen intervals that might, for instance but not necessarily, correspond to the set of tangent radii of the observation. This set of linear segments can be represented as a linear combination of triangular functions, as shown in **Figure 2**. These triangles $t_k(r)$ can be written as

$$\begin{aligned} t_k(r) &= \frac{r - r_{k-1}}{r_k - r_{k-1}} \chi_{]r_{k-1}, r_k[}(r) + \left(1 - \frac{r - r_k}{r_{k+1} - r_k}\right) \chi_{]r_k, r_{k+1}[}(r) \\ &= \frac{r - r_{k-1}}{r_k - r_{k-1}} \chi_{]r_{k-1}, r_k[}(r) + \frac{r_{k+1} - r}{r_{k+1} - r_k} \chi_{]r_k, r_{k+1}[}(r), \end{aligned} \tag{8}$$

where we use the characteristic function $\chi_\Omega(r)$, which takes the value 1 when $r \in \Omega$ and 0 otherwise and where $k = 1, \ldots, n$ enumerates the different nodes r_k. The first (second) term of expression (8) can be ignored at $k = 0$ ($k = n$, respectively). Any piecewise linear, continuous function f can then be written as a linear combination of the t_k:

$$f(r) = \sum_k a_k t_k(r). \tag{9}$$

The Abel transform $T_k(r_0)$ of each triangle t_k can be easily computed using I_{-1}, I_0 and I_1 from equations (6) and (7). The Abel transform (4) is linear for f and we thus have

$$F(r_0) = \sum_k a_k T_k(r_0). \tag{10}$$

Figure 3 shows the Abel transform of a triangular function. In this figure, the Abel transform $F(r_0)$ is zero for any value of r_0 larger than the upper boundary of the interval over which the triangle is defined. The Abel transform $F(r_0)$ varies rather smoothly, despite the discontinuous first derivative of the triangle function. Now, when $f(r)$ has to be estimated from line-of-sight integrated measurements G_j obtained for a set of radial distances $r_{0,j}$, $j = 1, \ldots, J$ (for simplicity, we assume that the $r_{0,j}$ are sorted by increasing r_0) one just has to minimize the chi-square expression

$$\chi^2 = \sum_{j=1}^{J} \left(G_j - \sum_k a_k T_k(r_{0,j}) \right)^2 w_j \tag{11}$$

using standard linear minimization techniques. The weights w_j will generally be set equal to the inverse of the variance and they will be the diagonal elements of the inverse of the variance matrix $\mathbf{V}_G$ of the measured G_j (which we assume do not co-vary). They may also be set to 1 for unweighted least squares fit. Indeed, under the assumption of homoscedasticity, the Gauss-Markov theorem states that an optimal estimation of the parameters is provided by the weighted least squares fitting. The suitable a_k's are thus obtained by solving the system

$$\boldsymbol{H}\,\vec{a} = \vec{b} \tag{12}$$

For $\vec{a}$, with

$$\begin{aligned} H_{ik} &= \sum_{j=1}^{J} T_i(r_{0,j})\, T_k(r_{0,j})\, w_j = (\mathbf{T}\,\mathbf{V}_G^{-1}\mathbf{T}^{+})_{ik} \qquad T_{ji} = T_i(r_{0,j}) \\ b_i &= \sum_{j=1}^{J} G_j\, T_i(r_{0,j})\, w_j \end{aligned} \tag{13}$$

Many terms of the sums of equation (13) are zero, as $T_k(r_{0,j}) = 0$ for any $r_{0,j} > r_{k+1}$. By solving system (12), F is adjusted to the set of observations $\{G_j, j = 1, \ldots, J\}$. The solutions of the system, a_k, are then used in expression (9) to construct the adjusted f. The quality of the solution of such an inverse problem can often be improved by applying Tikhonov regularization, especially when the problem is ill-conditioned. We outline here the principle of such regularization; details can be found, e.g., in Press et al. (1992). The key idea behind the Tikhonov regularization is to modify the quantity that is to be minimized by adding a contribution that penalizes a property of the fitted result that is considered as inappropriate. For example, if the result is expected to be fairly constant, we can add a term proportional to the square of the first derivative (or its integral) in order to penalize any solution with strong variations or, if the result is expected to be rather smooth (a special case being close to linear), we can attenuate possible noisy variations of the fitted function by adding a term proportional to the square of the second derivative (or its integral), to be represented in discrete form. This is indeed a way to protect the inversion procedure against the deleterious effects of noise. The usual method to regularize the fitted function is then to replace equation (12) by

$$(\mathbf{H} + \lambda\, \mathbf{Q})\, \vec{a} = \vec{b} \tag{14}$$

where λ can be viewed as a suitable weight applied to the regularization matrix **Q**, the other symbols keeping their original definition. The regularization matrix **Q** must now be determined. Press et al. (1992) provide **Q** suitable for equally-spaced observational points. The derivatives can then be approximated by (forward) finite differences of the fitting parameters, and the resulting regularization matrices are naturally simple and almost symmetric. Note that a sophisticated and very accurate method of computation of the derivatives is indeed not necessary as it would be the case in a solver for differential equations: we are only searching for an expression that penalizes a property that we consider a priori should remain small. We adapt the algorithm from Press et al. (1992) to the specific case of equation (10) in which the derivatives are not estimated by differences of the fitting parameters. We can write the second derivative of F computed at the observation points $r_{0,i}$ and pack them in a vector:

$$\vec{D} = \left.\frac{\partial^2 F}{\partial {r_0}^2}\right|_{r=r_{0,j}} = \sum_k a_k \left.\frac{\partial^2 T_k}{\partial {r_0}^2}\right|_{r=r_{0,j}} = \sum_k S_{jk}\, a_k = \mathbf{S}\, \vec{a} \tag{15}$$

where the components of the matrix **S** are

$$S_{jk} = \left.\frac{\partial^2 T_k}{\partial {r_0}^2}\right|_{r=r_{0,j}}. \tag{16}$$

The sum of the squares of the second derivative can then be written in matrix format as

$$D^2 = \vec{D}^{+}\vec{D} = \vec{a}^{+}\, \boldsymbol{S}^{+}\, \boldsymbol{S}\, \vec{a} = \sum_{i\,j\,k} a_k\, S_{ik}\, S_{ij}\, a_j \tag{17}$$

We may prefer to compute the integral of the square of the second derivative, which can be estimated numerically as

$$\begin{aligned} \int_{r_{0,1}}^{r_{0,J}} dr \left(\frac{\partial^2 F}{\partial {r_0}^2}\right)^2 &\simeq \sum_j \left(\sum_k a_k \left.\frac{\partial^2 T_k}{\partial {r_0}^2}\right|_{r=r_{0,j}}\right)^2 h_j \\ &= \sum_j \left(\sum_k a_k \left.\frac{\partial^2 T_k}{\partial {r_0}^2}\right|_{r=r_{0,j}} \sqrt{h_j}\right)^2, \end{aligned} \tag{18}$$

where h_j can be taken as $h_j = r_{0,j+1} - r_{0,j}$ (with $h_J = h_{J-1}$) or as any other suitable discretisation step length. The derivatives of the T_k can be estimated by any suitable mean: analytically or numerically (using a central difference scheme, for example). We can then define a matrix **S** by

$$S_{jk} = \left.\frac{\partial^2 T_k}{\partial {r_0}^2}\right|_{r=r_{0,j}} \sqrt{h_j}\,. \tag{19}$$

Formally, computing the sum of the square or the integral of the square of the second derivative can both be done similarly using expression (17). We now want to obtain the matrix **Q** of equation (14) in order to perform a minimization. We then need to compute the first derivatives of D^2 with respect to the a_k:

$$\frac{\partial D^2}{\partial a_l} = \frac{\partial}{\partial a_l}\left(\sum_{i\,j\,k} a_k\, S_{ik}\, S_{ij}\, a_j\right) = 2\sum_{i\,k} a_k S_{ik} S_{il} = 2\,\mathbf{S}^{+}\mathbf{S}\,\vec{a}|_l \tag{20}$$

so that we can define **Q** by

$$\mathbf{Q} = 2\,\mathbf{S}^{+}\mathbf{S} \tag{21}$$

We still have to determine the factor λ in equation (14). We follow Press et al. (1992) and chose

$$\lambda = Tr(\mathbf{H})/Tr(\mathbf{Q}), \tag{22}$$

where Tr(**A**) denotes the trace of matrix **A**. Note that the factor 2 in equation (21) is simplified out of equation (14) when adopting this value for λ.

The method outlined above is very general and it is not specifically designed for the case of cometary atmospheres. It was already introduced by Quémerais et al. (2006) for the study of the atmosphere of planet Mars. We will adapt the inversion method for cometary atmospheres in two steps: First, we will modify the regularization method, and second, we will modify the t_k introduced in equation (8).

The regularization method proposed occasionally suffers from a severe drawback: if the observed quantity and its derivatives vary over several orders of magnitude across the observed atmosphere (and this can be the case in cometary and planetary atmospheres), then D^2 will be dominated by the largest values, and regularization will become less efficient in those regions of the atmosphere where the emission rate (for example) is smaller, i.e. where regularization may be the most needed. We then change the regularization method by considering the a_k as a list of discrete values of a function $a(r)$, and we regularize the fit by minimizing its second derivative. Equivalently, we may consider the a_k as a suite and minimize its second-order discrete difference, with similar results. We can write $h_k = r_{k+1} - r_k$ ($h_n = h_{n-1}$) and use a simple finite difference scheme as an approximation for the second derivative

$$
\begin{aligned}
&\left.\frac{da}{dr}\right|_k \simeq \frac{a_{k+1} - a_k}{h_k} \\
&\left.\frac{d^2a}{dr^2}\right|_k \simeq \frac{\left.\frac{da}{dr}\right|_k - \left.\frac{da}{dr}\right|_{k-1}}{\frac{1}{2}(h_{k-1} + h_k)} \simeq \frac{2\,a_{k-1}}{h_{k-1}^2 + h_{k-1}h_k} - \frac{2\,a_k}{h_k h_{k-1}} + \frac{2\,a_{k+1}}{h_{k-1}h_k + h_k^2} \;(1 < k < n) \\
&\left.\frac{d^2a}{dr^2}\right|_{k=1} \simeq \frac{a_2 - a_1}{h_1^2} \qquad \left.\frac{d^2a}{dr^2}\right|_{k=n} \simeq \frac{a_{n-1} - a_n}{h_n^2}
\end{aligned} \tag{23}
$$

Expressions for $k = 1$ and $k = n$ are obtained by considering virtual values $a_0 = a_1$, $h_0 = h_1$ and $a_{n+1} = a_n$, $h_{n+1} = h_n = h_{n-1}$ and applying the expression given for $1 < k < n$. The vector collecting the second derivative values can then be written in matrix format using a tri-diagonal matrix, noting $q_k = 1/(h_{k-1}^2 + h_{k-1}\, h_k)$ and $v_k = 1/(h_{k-1}\, h_k + h_k^2)$:

$$
\begin{aligned}
&\vec{D}_a = \mathbf{B}_0\,\vec{a} \\
&B_0 = 2\begin{pmatrix}
\frac{-1}{2h_1^2} & \frac{1}{2h_1^2} & & & & & \\
q_1 & -q_1 - v_1 & v_1 & & & & \\
 & q_2 & -q_2 - v_2 & v_2 & & & \\
 & & \ddots & \ddots & \ddots & & \\
 & & & q_{n-1} & -q_{n-1} - v_{n-1} & v_{n-1} & \\
 & & & & q_n & -q_n - v_n & v_n \\
 & & & & & \frac{1}{2h_n^2} & \frac{-1}{2h_n^2}
\end{pmatrix}
\end{aligned} \tag{24}
$$

The numerical scheme adopted in equation (23) makes $\mathbf{B}_0$ tri-diagonal and diagonally dominant. We can now write the sum of the squares of the second derivatives as in equation (17):

$$
D_a^2 = \vec{a}^+\,\mathbf{B}_0{}^+\mathbf{B}_0\,\vec{a}. \tag{25}
$$

Its derivative with respect to a_l is again obtained as in equation (20):

$$
\frac{\partial D_a^2}{\partial a_l} = \frac{\partial}{\partial a_l}\left(\sum_{i\,j\,k} a_k\,B_{0_{ik}}\,B_{0_{ij}}\,a_j\right) = 2\sum_{i\,k} a_k B_{0_{ik}} B_{0_{il}} = 2\,\mathbf{B}_0{}^+\mathbf{B}_0\,\vec{a}\big|_l \tag{26}
$$

And the regularization matrix can now be written

$$
\mathbf{Q} = \mathbf{Q}_{0_a} = 2\,\mathbf{B}_0{}^+\mathbf{B}_0. \tag{27}
$$

The multiplicative factor λ of equation (14) is again given by equation (22), and we can transform $\mathbf{B}_0$ the same way as $\mathbf{S}$ in equation (19) in order to numerically compute the integral of the square of the second derivative, which can also be viewed as a weighted sum of the square of the elements of $\vec{D}_a$ with the lengths of the interval over which the triangular elements t_k are defined (equation 8) chosen as weights. The new matrices $\mathbf{B}$ and $\mathbf{Q}_a$ become then

$$B_{ki} = B_{0_{ki}}\sqrt{h_k}$$
$$\mathbf{Q}_a = 2\,\mathbf{B}^{+}\mathbf{B}. \tag{28}$$

We now turn to the task of defining new “triangular” elements instead of the expression given in equation (8). Our purpose is to find an expression that would be more suitable to the description of the constituents of a cometary atmosphere. In a first approximation, the Haser model given by equations (1), (2) and (3) for inert, mother and daughter species, respectively, provides an adequate description of the distributions of these constituents. We want to derive triangular elements whose Abel transform can be calculated analytically, in order to reduce the computational cost. The presence of the exponential function in expressions (2) and (3) severely complicates the analytic computation of the indefinite integral built from the Abel transform. We can however compute those primitives for negative powers of *r*, which points at the Haser model for inert molecules, proportional to $1/r^2$. We thus define new “triangular” elements, using the triangles t_k from equation (8) as

$$u_k(r) = \frac{t_k(r)}{r^m} \quad m > 0 \tag{29}$$

Quite obviously, we will choose $m = 2$ in the case of a cometary atmosphere so that the $1/r^2$ dependency that appears in the Haser model is explicitly present in the triangular elements. We write their Abel transforms U_k to use them instead of the T_k in the definitions of matrices **H** and **S** in equations (13), (16) and (19). The u_k so defined do always reduce to a linear combination of negative powers of r (over bounded intervals). Analytical computation of their Abel transform thus only requires us to know the indefinite integrals of the form

$$L_m = \int dr\, \frac{r}{\sqrt{r^2 - r_0^2}}\, r^{-m} \tag{30}$$

An integration by parts again shows that the L_m satisfy a recurrence relation:

$$(m-1)L_m - m\, r_0^2\, L_{m+2} + \frac{\sqrt{r^2 - r_0^2}}{r^m} = 0$$
$$L_0 = \sqrt{r^2 - r_0^2}$$
$$L_1 = \operatorname{arcosh}\left(\frac{r}{r_0}\right) = \ln\left(\frac{r}{r_0} + \sqrt{\frac{r^2}{r_0^2} - 1}\right) \tag{31}$$
$$L_2 = \frac{1}{r_0}\operatorname{arctg}\left(\sqrt{\frac{r^2}{r_0^2} - 1}\right) = \frac{1}{r_0}\arccos\left(\frac{r_0}{r}\right)\ .$$

L_0 and L_1 can be directly obtained from equation (30); L_2 is found after the variable change $s = \sqrt{\frac{r^2}{r_0^2} - 1}$ and using a trigonometric identity to transform the arctangent into an arccosine. Notice that the recurrence relation cannot be used to deduce L_2 from L_0 as the term in L_2 vanishes for $m = 0$. One possibility to further improve the triangular elements would be to apply an offset, replace r^{-m} by $(r-a)^{-m}$ in expression (29) and to call upon Laurent series with an offset. This choice could be suitable in the case of a planetary atmosphere, for which the extent of the emitting layer is small compared with the planet radius. Indefinite integrals of the form

$$\int dr \, \frac{r}{\sqrt{r^2 - r_0^2}} \, t_k(r) \frac{1}{(r-a)^m} \qquad 0 < a < r_0 \tag{32}$$

can always be reduced to a linear combination of indefinite integrals of the form

$$W_m = \int dr \, \frac{1}{\sqrt{r^2 - r_0^2}} \frac{1}{(r-a)^m} \tag{33}$$

completed with the first elements of the suite of integrals I_n given by equations (6) and (7) when $m < 3$. These integrals satisfy again a recurrence relation and are also related by a simple derivative with respect to the parameter a. We will not use that refinement here. We nevertheless report the analytical results and developments in appendix 1, as some of the computations could be useful for the studies of planetary atmospheres.

In this study, we will only investigate the use of elements t_k and u_k with $m = 2$ (equations (8) and (29)) to represent emission profiles in cometary atmospheres, assuming spherical symmetry.

When uncertainties affecting the observation are known, the weights w_j in equation (11) can be taken as $1/\sigma_j^2$ i.e., the inverse of the variances affecting the observational points. As the fitted parameters a_k are obtained by applying formulas of linear algebra, error propagation techniques can be used to obtain the variance matrix of the a_k's and the standard deviation (i.e., the uncertainty) of the fitted profiles. We remind here the standard general formulas needed to obtain the desired uncertainties. If we denote by $\mathbf{V}_G$ the variance matrix of the observation (which in our case will be a diagonal matrix $\mathrm{diag}(\sigma_j^2)$) we can obtain the variance matrix $\mathbf{V}_a$ of the fitted parameters by noting that, formally, they are computed by just multiplying the observation vector $\vec{G}$ by a matrix M:

$$\vec{a} = \mathbf{M}\vec{G} \tag{34}$$

In this case the variance matrix $\mathbf{V}_\mathrm{a}$ can be written in matrix form as

$$\mathbf{V}_a = \mathbf{M}\,\mathbf{V}_G\,\mathbf{M}^+. \tag{35}$$

Matrix $\mathbf{M}$ is deduced from equations (13) and (14) as:

$$\mathbf{M} = (\mathbf{H} + \lambda\,\mathbf{Q})^{-1}\mathbf{T}^+\mathbf{V}_G^{-1}. \tag{36}$$

The parameter λ can be set to 0 when no regularization is applied. This can, however, lead to numerical problems when **H** is ill-conditioned. In contrast, introducing the regularization warrants that the problem will be well-conditioned and the inverse matrix will be computable. Because the Abel transform of a triangular element (**Figure 3**) extends from the nucleo-centric distance where this element is defined down to $r_0 = 0$, the a_k are expected to co-vary and $\mathbf{V}_a$ will not be diagonal. Its diagonal elements are nevertheless the most important ones as they determine the (square of the) uncertainties affecting the fitted a_k's. Once the covariances and uncertainties affecting the a_k's have been obtained, standard error propagation formulas can be used to derive the uncertainties of the fitted F and f from equations (9) and (10). If we collect the estimated values of F at each $r_{0,j}$ in a vector, the variances of the F_j are then the diagonal elements of matrix $\mathbf{T}^{+}\mathbf{V}_a\mathbf{T}$, and a similar expression can be obtained for the f_k.

3. THEORETICAL TESTS

3.1. Inert species profiles

Before analyzing real observations, we apply our method to theoretical nucleo-centric profiles of the Abel transform F, which is what we use to retrieve the emission rate profile. We will also check that the inversion method gives appropriate results. **Figure 4** shows the line-of-sight integrated profile F obtained from an emission rate varying as $1/r^2$, i.e., it is proportional to the variation of L_2 given in equation (31) between r_0 and ∞, and thus varies as $1/r_0$. Panel b shows the emission rate profile f obtained by numerical inversion of F given at a restricted set of nucleo-centric distances, without regularization, using purely triangular elements t_k as given by equation (8) (triangles) and elements u_k built by dividing each t_k by r^2 (equation (29), with $m = 2$). The corresponding line-of-sight integrated values are shown in Figure 4a using the same plotting symbols. At first glance, both methods seem to give a satisfying inversion, showing that the inversion method correctly retrieves the expected emission rate. **Figures 4c** and **4d** show the absolute value of the relative difference between the numerically-inverted profiles and the input local emission rate. Inversion using elements u_k performs obviously better. This is expected as the chosen elements better match the emission rate profile corresponding to F. **Figure 5** shows the same as **Figure 4** with regularization. In the case of purely triangular elements, regularization appears as counter-productive over this particular profile, while it slightly reduces the absolute deviation from the correct values in the case of elements consisting in triangles divided by r^2. Truncation of the profiles at large nucleo-centric distance is an obvious source of error. Moreover, these profiles are somewhat artificial: they were built using a set of nucleo-centric radii that are spaced following a power law, so that the discrete profiles appear as regularly-spaced points in a log-log diagram. Real data will not resemble those profiles: in general, observations are regularly spaced versus nucleo-centric distance, and the signal is contaminated by noise.

Figure 6 shows a more realistic (albeit still theoretical) case, using regularly spaced nucleo-centric bins, and including noise contamination of the Abel transform F. **Figure 6a** shows the theoretical profile (dashed line) and the noisy profile used as input to the Abel inversion algorithm (solid line). **Figure 6b** shows the absolute value of the relative difference between the dashed and solid lines of **Figure 6a**. **Figure 6c** shows the ideal theoretical line-of-sight (l.o.s.) integrated profile (dotted line) with the l.o.s. integrated profile fitted using triangular elements divided by r^2, with and without regularization (long and short dashes, resp.). The uncertainties over the fitted curves that result from noise propagation, are represented as dark (light) shades for the non-regularized (regularized, respectively) profile. Figure 6d shows the theoretical local emission rate (dotted line) and the nonregularized (short dashes) and regularized (long dashes) fitted profiles. Again, the ±1σ uncertainties over the fitted profiles are represented as dark (light) shade for the non-regularized (regularized, resp.) fitted emission rate. Both the regularized and nonregularized fits nearly retrieve the exact value, but the benefit of regularization clearly appears, as the long-dash curve is smoother and thus broadly closer to the correct values. This is also reflected by the much smaller uncertainties affecting those values, especially at large nucleo-centric distance, where F becomes small. As it can be expected, both the boundary effects and the large simulated noise impair the quality of the fitted profile near the boundary at 20000 km. **Figures 6e** and **6f** show the same as **Figures 6c** and **6d**, respectively, except that purely triangular elements were used in the inverse Abel transform fit. The quality of the results shown in **Figures 6e** and **6f** is obviously not as high as those from **Figures 6c** and **6d**. Regularization even appears as counterproductive in this case. This naturally results from the less adapted shape of the elements used here. It thus clearly appears that the best choice is to use elements u_k with $m = 2$ to study cometary profiles, and to apply the regularization procedure. The regularization used here aims at minimizing the integral of the square of the second derivative of the fitted a_k (equations (23) to (28)). Regularization based on the minimization of the sum of the square of the second order discrete difference of the a_k gives fairly similar results. On the other hand, regularization based upon the second derivative of the fitted F (not shown) performs worst, as anticipated above. We note that the argument that we developed to suggest that minimizing the integral of the second derivative of F might not be the best choice for cometary atmospheres could also apply to the regularization applied to the fitting parameters obtained using purely triangular elements. Our best choice finally appears to be to use triangles divided by r^2 and regularization operating directly on the a_k because the $1/r^2$ multiplication partly corrects for the drawbacks of the alternative regularization choices.

3.2. Disturbed inert species profiles

The tests presented up to now used emission rate profiles proportional to $1/r^2$. This choice does perfectly correspond to the u_k elements used to realize the fits and one may wonder if these elements would still be appropriate if the emission profile departs from this best possible case. We thus constructed an emission rate profile consisting of a $1/r^2$ profile to which a bump (idealized by a Gaussian curve) was added. We carefully performed the l.o.s. integration numerically (using a very high space resolution and extending the emission rate profile far beyond 20000 km) and used the inversion method with that l.o.s.-integrated profile as input. The results are shown in **Figure 7a** and **b**. Regularized inversion with triangles divided by r^2 is used. The bump added to the profile is indeed retrieved, although the match is not perfect (such a disturbance of the profile is certainly more severe than any disturbance we may imagine to find in a real cometary observation). The fitted emission rate becomes disturbed beyond the bump, because the fitting parameters co-vary and are disturbed by the bump and by noise. In this extreme test, the propagated noise then becomes a poorer estimator of the uncertainty over the local emission rate profile, and the fitted profile shows erratic oscillations around the correct value.

We also performed another important test: the inverse Abel transform of a profile varying as $1/r$ (i.e. for which we expect to retrieve the local emission rate varying as $1/r^2$) to which a constant offset is added. This test is important because cometary observations have a contribution from the background sky, which can often be considered as constant across the whole coma, although some observations have a sky background that varies across the image, especially if the bright moon approaches the field of view. Subtraction of this offset is often a difficult task, and thus a source of uncertainty. The theoretical expression of the inverse Abel transform does however only involve the first derivative of F so that, if it could be applied to real data, it would give a result independent of the constant offset due to the sky background. Unfortunately, real data are noisy, binned over a discrete set of nucleo-centric distances, and spatially limited, so that we have to rely on numerical methods that may be sensitive to the offset. **Figure 7** shows our simulation of an observation contaminated by an offset in panels c and d. The noise applied to the input l.o.s.-integrated emission (F) is not included in the plot for clarity. The constant added to the $\sim 1/r$ l.o.s.-integrated profile has been purposely chosen very large, causing a doubling of F already near $r = 1000$ km. The fitted l.o.s.-integrated profile does not seem to correctly retrieve the augmented profile (the dash-dot-dot-dot line). It rather seems to be offset by a larger amount, with a rapid decrease near the boundary at 20000 km. The emission rate profile, however, does more closely correspond to the $\sim 1/r^2$ profile, except near the boundary at 20000 km. It is surprising that, despite the ~1 order of magnitude contamination of F near 10000 km (already a factor 2 near 1000 km), and despite the erroneous retrieval of F at large nucleo-centric distance, the emission rate is rather correctly retrieved over a broad part of the profile. This stems from the fact that two l.o.s.-integrated profiles differing from each other by only an additive constant have the same inverse Abel transform. The numerical inversion technique developed here is not fully insensitive to the added constant. Consequently, the good strategy to follow when analyzing an observed coma would be to estimate the constant background of the sky as accurately as possible, subtract it from the observed cometary emission and apply the Abel inversion, knowing that the result will be only weakly sensitive to a misestimate of the constant background, across a large portion of the observed coma. This advantage alone can already be seen as a good reason for inverting the l.o.s.-integrated observation and study the emission rate itself. It must be added that all the theoretical tests proposed here were performed using as many fitting elements as pseudo observation points (i.e. $J = K$ and $r_j = r_{0,j}$ in the formalism developed in the preceding section). Other choices are possible and can sometimes give even better results. Quite obviously, least squares fitting is, in principle, a method that is generally used to determine a relatively small number of relevant parameters using a larger number of observations, increasing the number of observation points leading to smaller uncertainties over the fitted parameters. An interesting option is also to use fitting elements centered at nucleo-centric distance larger than that of the last point of the F profile, because the Abel transform of these elements will anyway extend to lower nucleo-centric distance. This choice could be particularly interesting when the signal-to-noise ratio remains very good across the whole observed profile. In principle, regularization could even allow us to “fit” more elements than the number of observation points: the matrix $\mathbf{H} + \lambda\mathbf{Q}$ (equation (14)) would generally not be singular in that case. However, it is illusory to expect to obtain meaningful results using that choice: one can hardly expect to retrieve more information than what stands in the data. The result would rather reflect some kind of additional "information" introduced in the system by the regularization.

3.3 Daughter species profiles.

Similar tests were conducted for emissions having a radial profile represented by a Haser model for daughter species characterized by realistic scale lengths L_p = 50000 km and L_d = 120000 km. We found that using fitting elements located at nucleocentric radius larger than that of the outermost point of the simulated observed profile does improve the quality of the fitted emission rate near the outer boundary of the radial range of the observation. When the interval covered by the fitting triangular elements is restricted to that of the radial range of the observation, the emission rate retrieved by the inversion method is overestimated, compared with the expected emission rate following a Haser profile for daughter species. This can be understood as follows: the l.o.s. integration of the emission includes contributions from the emission originating from altitudes above the tangent point. Truncation of the emission rate profile removes contributions to the l.o.s. integration that would be necessary to properly represent the (simulated) observation near the outer boundary of the profile. The least squares fit algorithm compensates for this defect by overestimating the emission rate in the last bins of the adjusted profile. Consequently, considering extra triangular elements beyond the tangent radius of the outermost observation (but still keeping the total number of elements lower than the number of points of the observed profile) introduces contributions that allow for a better retrieval of the emission rate near the outer boundary of the observed, l.o.s. integrated profile. However, beyond some radius, the fitted emission rate can become negative, which does obviously not make any physical sense. Conclusions regarding the emission rate profile at cometocentric radii larger than the tangent radius of the outermost observation can thus not be considered safe and better had to be avoided. Given that the inclusion of those extra bins is not to extend the range of validity of the inverted profile beyond the radius of the last observed point but rather to introduce a few degrees of freedom in the fit procedure to better model the observation at large nucleocentric distance, only a few extra bins suffices to improve the fit. In our test, some 10-15 extra bins extending the grid by some 1/2 - 2/3 L_d revealed efficient.

The tests conducted for the case of daughter species following a Haser model also show that the numerical Abel inversion does, at least partly, remove the effect of a constant background that might contaminate an observed profile. Numerical inversion uses a discrete representation over a truncated profile. One should not expect miracles though and hope the numerical inversion would remove the constant background contamination the way the analytical inverse Abel transform would do over an infinite radial range. There is a benefit in performing the numerical inverse Abel transform, but this benefit is not as large as the theoretical result of equation (5) might suggest.

It is common practice in cometary data analysis to determine the parameters of a Haser model representative of the observation using a least squares fit to the observation. As the emission rate profile can be estimated using a numerical inverse Abel transform applied to the data, one may wonder whether it is preferable to adjust the Haser model parameters directly on the observed profile rather than on the emission rate profile deduced from the inversion. We test this issue over Haser profiles of known parameters.

In a least squares fit procedure applied to a l.o.s. observation, the l.o.s. integration of the Haser model needs to be computed as well as the derivative with respect to the Haser parameters. We found the analytical expression of the l.o.s. integral of the Haser model for mother and daughter species. For least squares fitting purposes, we can express the Haser model for daughter species as $q_d = 1/L_d$, $q_p = 1/L_p$ and $Y = Q/(4\pi\,v)\,L_d/(L_d - L_p)$. One can equivalently use (Y, q_p, q_d) or (Y, L_p, L_d) as the fitting parameters, and the optimal fit is rapidly obtained noting the Haser radial profile $h(r)$:

$$
\begin{aligned}
&h(r) = Y\big(\exp(-q_d r) - \exp(-q_p r)\big)/r^2 \\
&H(r_0) = 2\int_{r_0}^{\infty} dr\, \frac{r}{\sqrt{r^2 - r_0^2}}\, h(r) = 2\frac{Y}{r_0}\big(P(q_d r_0) - P(q_p r_0)\big) \\
&P(a) = \int_1^{\infty} dx\, \frac{x}{\sqrt{x^2-1}} \frac{\exp(-a\,x)}{x^2} \\
&\qquad = \frac{\pi}{2}\Big(1 - a\big(B_K(0,a)\,S_L(-1,a) + B_K(1,a)\,S_L(0,a)\big)\Big) \qquad (37) \\
&\frac{\partial H(r_0)}{\partial Y} = \frac{H(r_0)}{Y} \quad ; \quad \frac{\partial H(r_0)}{\partial q_d} = -2\,Y\,B_K(0, q_d r_0) \quad ; \quad \frac{\partial H(r_0)}{\partial q_p} = 2\,Y\,B_K\big(0, q_p r_0\big) \\
&or\ \frac{\partial H(r_0)}{\partial L_d} = 2\,\frac{Y}{L_d^2}\,B_K(0, r_0/L_d) \quad ; \quad \frac{\partial H(r_0)}{\partial L_p} = -2\,\frac{Y}{L_p^2}\,B_K\big(0, r_0/L_p\big)
\end{aligned}
$$

where B_K(n,x) is the modified Bessel function of the second kind (Bessel-K) and S_L(n,x) is the modified Struve function (also called the Struve-L function), which can be evaluated from a fast-converging series (Abramowitz and Stegun, 1972). Details regarding the calculation of P(a) can be found in appendix 2 (as well as the series for the S_L function). The Abel transform of the Haser model for mother molecules can obviously be computed as well using function *P(a)* given in equation (37).

The Haser parameters of a radial profile for daughter species are estimated by accounting for a simulated noise and the possible presence of a constant background contribution in the simulated observation. This simulated radial profile is computed using the result of equation (37), contaminated by a Poisson noise and a constant offset background, and inverted using the numerical inverse Abel transform. The Haser parameters $L_{p,los}$ and $L_{d,los}$ are estimated using a Levenberg-Marquardt method applied to the simulated observation, while $L_{p,em}$ and $L_{d,em}$ are fitted over the emission rate determined by the numerical inverse Abel transform. When no background is included in the simulated observation, both methods give similar values for L_p and L_d, although $L_{p,los}$ and $L_{d,los}$ seem to fall somewhat closer to the exact values used as an input. However, when a residual background is present in the simulated profile, it is $L_{p,em}$ and $L_{d,em}$ that seem to be closer to the expected values. The presence of a small positive offset reduces the slope of the simulated l.o.s. integrated profile at large cometocentric distances. This leads to an increase of the fitted $L_{d,los}$ and a reduction of $L_{p,los}$. Because the numerical inverse Abel transform partly removes the effect of the constant offset, the fitted $L_{p,em}$ and $L_{d,em}$ are less disturbed and they fall closer to the exact value. Naturally, if the nucleocentric profile does not rigorously follow a Haser model, only an inversion of the observed profile can estimate the emission rate profile.

4. APPLICATION TO OBSERVED COMETARY ATMOSPHERES

In this section, we will apply the method derived in section 2 and tested in section 3 to real cometary data obtained using the TRAPPIST telescope (Jehin et al., 2011). TRAPPIST is a 60-cm robotic telescope installed in 2010 at La Silla observatory. The telescope is equipped with a 2Kx2K thermoelectrically-cooled FLI Proline CCD camera with a field of view of 22'x22' and a plate scale of 1.302"/pix. A set of narrow-band filters isolating the main emission bands in the optical spectrum of comets, i.e., OH, NH, CN, C_3, and C_2, as well as emission-free continuum regions at four wavelengths (Farnham et al., 2000) is permanently mounted on the telescope.

The reduction method applied to the TRAPPIST data has been extensively described by Opitom et al. (2015) and will only be briefly summarized here. TRAPPIST images are reduced following a standard procedure using frequently updated master bias, flat and dark frames. The removal of the sky contribution may be problematic for extended objects. However, for the comets considered hereafter, the TRAPPIST field of view was always wide enough to determine the sky contribution from parts of the images free of cometary contribution. We first determine the location of the comet's optocenter in the image (using the Iraf task imcntr). Second, we determine the closest distance from the coma optocenter where each image is free of cometary emission, and measure the median sky level at this nucleocentric distance, which is subtracted from the image. We then derive the median radial brightness profile for each image. The use of a median profile eliminates the contribution of background stars. Even though narrowband filters have been carefully designed to isolate specific molecular emissions, they are contaminated by the underlying sunlight reflected by the dust. The dust subtraction is thus a very important step in the data reduction. We use images of the comet in the BC filter (i.e. at 444.9 nm) to obtain the dust radial profile, scale it depending on the contamination in the gas filter, and subtract it from the gas profile. Continuum frames used for the dust subtraction are usually taken during the same hour as the associated frame to avoid changes in the observing conditions or in the rotational state of the comet. Regular observations of narrowband photometric standard stars listed in Farnham et al. (2000) allow us to determine each filter zero point and extinction coefficients used to convert count rates into fluxes.

4.1. Estimation of the uncertainties

We derive the local rates of various cometary emissions from their l.o.s.-integrated observations, i.e., from their Abel transform. Estimating the uncertainties affecting the observations is often difficult. Some of these uncertainties will not have a dramatic effect over the range of local emission rates that we will estimate: a small misestimate of the sky background has nearly no effect over the result of the inverse Abel transform, as was explained in section 3. We thus adopt a rather pragmatic method to estimate the uncertainties over the observed emission profile. If we note G_j the observation of a given emission, obtained under a nucleo-centric tangent radius $r_{0,j}$ (all sorted by increasing tangent radius), the uncertainty σ_j affecting this observation is directly estimated from the neighboring observations using the following method. First, we smooth the observed radial profile to obtain the set of numbers G_j^* ($j = 1, \ldots, J$). This smoothing is realized using a Savitsky-Golay filter (Savitsky and Golay, 1964) applied to the logarithm of the G_j's. This choice is made because of the fast decrease rate of the l.o.s.-integrated cometary profile: the logarithm of the G_j's varies much slowlier than the original data. One can view the Savitsky-Golay filtering method as a generalization of the boxcar smoothing. In a boxcar smoothing directly applied to the data G_j , G_j^* would be the average of the G_i's over i varying from $j - d$ to $j + d$, the size of the smoothing "box" being $2d + 1$ elements. This is equivalent to replacing the G_j's by a zeroth order polynomial fitting the neighboring elements of G_j. The Savitsky-Golay filter generalizes this idea: a polynomial of arbitrary degree chosen by the user is fitted over a set of elements of the array of data centered on G_j, the set having a width $2d + 1$ (chosen by the user as well). It reduces to a convolution with a kernel (that we will denote $\text{Ꝁ}_{q,d}$) that depends on the chosen degree of the polynomial (which we will denote q) and the width over which the smoothing is realized (namely d). Here, instead of applying the filter directly to the data, we apply it to the logarithm of the data and compute the exponential of that smoothed set. Once the smoothed array G_j* is obtained, we use it to locally de-trend the observed profile G_j and compute the mean and standard deviation over that restricted interval, as if the de-trended result gave several estimates of G_j:

$$
\begin{aligned}
&G^* = \exp\big(\ln(G) \star \text{Ꝁ}_{q,d}\big) \\
&m_j = \frac{1}{2g+1} \sum_{i=j-g}^{j+g} G_i \frac{G_j^*}{G_i^*} \qquad (j = 1, \ldots, J) \\
&\sigma_j = \sqrt{\frac{1}{2g+1} \sum_{i=j-g}^{j+g} \left(m_j - G_i \frac{G_j^*}{G_i^*}\right)^2} \qquad (j = 1, \ldots, J)
\end{aligned}
\tag{38}
$$

In equation (38), the operator $\star$ stands for the convolution product and g is a positive integer which defines the number of adjacent measurements used to estimate the uncertainties over the G_j's. It must be chosen sufficiently large to allow for a reasonably meaningful estimation of the uncertainty, but it must also remain small enough so that the set of de-trended measurements $G_i\, G_j^*/G_i^*$ ($j - g < i < j + g$) can be viewed as several estimates of G_j, which is obviously never strictly true. Moreover, the sums appearing in (38) present problems near the boundaries of the measurements (near $j = 1$ and $j = J$). The sums need to be truncated accordingly, and the denominator amounting to the number of elements actually involved in the sum must be corrected. We performed numerical tests that tend to indicate that the method of equation (38), when applied to a profile typical of a cometary atmosphere (i.e., the Abel transform of a Haser model) with known uncertainties (i.e., a randomly generated noise with a standard deviation proportional to the square root of the profile) tends to somewhat underestimate the uncertainties. In our tests, that bias could be corrected for by applying a safety factor of 1.2 to the estimated σ_j so that the estimated uncertainties better correspond to the known noise used in the numerical test, although one should not expect this nearly unit factor would dramatically influence the results. Yet, there is another subtlety that has to be accounted for in these expressions. The Savitsky-Golay filter reduces to a (numerical) convolution product of the (logarithms of the) G_j's with an appropriate kernel. Close to the boundaries, and in particular close to the inner boundary (i.e., for $r_{0,j}$ near 0), truncation of the convolution degrades the quality of the smoothed profile G_i^*, leading to unacceptably wrong (over)estimates of σ_j. We correct this problem by scaling σ_j ($j < j_{\mathrm{crit}}$) along the square root of G_j, with j_{crit} being the index of the first j at which the convolution product and the estimates of equation (38) can be carried out without truncation problem: $j_{\mathrm{crit}} = d + |d - g|/2$. This scaling choice makes sense when the uncertainties are mostly due to the Poisson noise affecting the measurements.

Figure 8 shows how this method of noise estimation performs when applied to an ideal profile with known uncertainties. We generate a l.o.s.-integrated Haser profile discretized over 500 equally-spaced nucleo-centric distances. We then compute its square root that we use as a standard deviation to generate a Poisson noise to be applied to the ideal Haser profile (dotted line in Figure 8a). We apply a Savitsky-Golay filter (as outlined in equation (38)) using a width of 21 points and a fifth degree polynomial, i.e., with $d = 10$ and $q = 5$ (long dashed line in Figure 8a). Obviously, the smoothed profile is a poor estimate of the l.o.s.-integrated emission rate at low nucleo-centric distance. We then compute the local average and standard deviation as explained in equation (38) over 31 neighboring points (i.e., with $g = 15$), and applying the safety factor of 1.2. The result is shown using the long dashes in panel b. Quite obviously, this estimate of the uncertainty is very wrong near the inner boundary, while it fairly follows the dotted line at larger nucleo-centric distance. We then apply the square root scaling at low nucleocentric distance as explained above to obtain the uncertainties in the part of the profile where the filter-based method does not suffice (short dashed line in Figure 8b). The estimate of the uncertainty is then fairly good all over the profile. Incidentally, the uncertainties are somewhat underestimated at low nucleo-centric distance because the uncorrected method produced a slightly underestimated uncertainty near j_{crit}, but overall, the uncertainties are recovered in an acceptable manner. The method used to estimate the noise level is actually independent of the inverse Abel transform itself. It has been introduced to derive values for the uncertainties in the χ^2 expression (11) and for the error propagation procedure that is used to estimate the uncertainties of the fitting parameters.

Obviously, the reliability of any least squares fitting method improves when the uncertainties are accounted for. Indeed, weighting with adequate uncertainty estimates helps to prevent an overfitting of the noise affecting the large contributions to the profile (i.e., at low nucleocentric distance) at the expense of the fitting of physically meaningful signatures that may arise at large nucleocentric distance where the measured intensity is much smaller. From that standpoint, a rough estimate of the uncertainties suffices.

4.2. Data analysis

We first apply our methods to observations of comet 103P/Hartley 2 obtained with TRAPPIST on November 7, 2010. Comet 103P/Hartley 2 was discovered in 1986. It is a Jupiter Family comet with a period of 6.47 years. 103P/Hartley 2 is one of the few comets that have ever been visited by a spacecraft: it was the target of a close flyby by the NASA Deep Impact space probe on November 4, 2010. In parallel to the flyby, an extensive space-borne and ground-based campaign was initiated to complement the in-situ observations. The comet passed within only 0.12au from the Earth two weeks before the flyby, allowing its coma to be sampled with high precision from the ground. We analyze the emission of molecule CN at 387 nm, i.e., the R branch of the (0-0) band of the B $^2\Sigma^+$ - X $^2\Sigma^+$ transition. In comets, the CN radical is predominantly produced by photo-dissociation of molecular HCN (Fray et al., 2005) (another possibility would be by dissociative recombination of HCN^+ ions). Excitation of the B $^2\Sigma^+$ - X $^2\Sigma^+$ system of bands is due to absorption of the solar light and its analysis should ideally account for the presence of the Fraunhofer bands in the solar spectrum (Arpigny, 1964).

Figure 9 shows the inversion results. The flux was measured at 723 different nucleo-centric distances and we used 242 triangular elements (equation (29)), i.e., ~1/3 of the number of points in the observed flux profile. A few triangular elements were added at radial values beyond the last point of the observed profile, for the reasons explained at the end of section 3. Regularization was applied on the integral of the second derivative of the fitting parameters (equation (28)). Figure 9a shows that the method produces a good fit of the observed flux; Figure 9b furthermore shows that the emission rate is reconstructed with very small uncertainties. Please notice that the (differential) flux is given per steradian, so that a factor of 4π is applied after Abel inversion to retrieve the volumetric emission rate. Clearly, the uncertainties that we retrieve are somewhat underestimated at very large nucleo-centric distance: the small increase of the emission rate near 90000 km does not seem to be realistic, and it probably results from a small shoulder seen in the observed flux near that nucleo-centric distance. We also determined a Haser model by least squares fitting over the emission rate, using the Levenberg-Marquardt method. Its characteristic lengths are L_p = 17500 km and L_d = 70100 km. We deduce the effective production rate Q_{HCN} (assuming that dissociation of HCN is the only source of CN, which may be an oversimplification) associated with this profile obtained while comet 103P/Hartley 2 was at a heliocentric distance of r_{H} = 1.07 ua, moving with a radial velocity of $\dot{r}_H$ = 3.2 km/s. We use the g-factor $g_{\mathrm{CN}} = 3.44\times10^{-13}$ erg s^{-1} molecule^{-1} based on the study of Schleicher (2010), which accounts for both the heliocentric distance and the radial velocity (important for the Swings effect). Assuming an expansion velocity of 1 km/s, we estimate that $Q_{HCN} = 2.68 \times 10^{25}$ particles s^{-1}. This number must be considered with care, as the Haser model relies on oversimplified assumptions. We compared these numbers with those obtained by fitting the Haser model directly using the observed flux, again using the Levenberg-Marquardt method. A fast implementation of the fit is possible as, for a Haser model, all the needed quantities can be computed analytically using the results of equation (37).

The fit realized directly over the observed flux gives $L_p^{(F)} = 2.16\times10^4$ km, $L_d^{(F)} = 4.9\times10^4$ km and $Q_{HCN}^{(F)} = 3.22\times10^{25}$ particles s^{-1}, which slightly differ from the values obtained above from the emission rates. The HCN production rates inferred for the different comets considered in this study are listed in **Table 1**. It must be noted that after adding a constant offset of 1.06×10^{-5} erg cm^{-2} s^{-1} sr^{-1} to the observed flux prior to fitting the Haser model, we retrieve very closely the same characteristic lengths and production rates than for the fits realized over the emission rates. This highlights once more that a small offset affecting the observed flux can have significant consequences (although not dramatic in this case): the fitted Haser parameters are sensitive to an offset applied to the observed flux (when the fit is realized directly over the flux), but the Abel-inverted flux (i.e., the emission rate) is nearly insensitive to a small offset. The difference between the values of the fitted parameters may be due to an overestimate of the sky background that was subtracted, which corresponds to an equivalent flux of 6.4×10^{-5} erg cm^{-2} s^{-1} sr^{-1}. It must, however, also be emphasized that comet Hartley 2 may well have an extended source region with a not well-determined size (A'Haern et al., 2011). This is an obvious departure from the hypothesis of the classical Haser model, mostly important near the nucleus, and that influences the fitted characteristic lengths. In addition, the dynamics of the acceleration of the gas produced by the cometary nucleus takes place in a volume extending several tens of kilometers away from the nucleus, as shown by the Monte Carlo simulations of the expanding coma (Tenishev et al., 2001, 2008, Rubin 2001, Combi, 1996). As a consequence, Haser model cannot be valid within some distance from the nucleus, even in the absence of outgassing from dust grains, which further worsens the correspondence with the Haser model when present. On the other hand, the numerical inverse Abel transform does not rely on any particular assumption concerning the shape of the profile of the coma (except for the assumption of spherical symmetry), so that the presence of an extended source or any other signature in the radial profile (providing that it is large enough to be resolved by the observing instrument) does not impinge on the quality of the results of the method itself. Anyway, determining the properties of the coma near a comet's nucleus remains challenging, because a feature needs to fill at least 2-4 pixels of the observed profile to be properly analyzable, due to the limits imposed by the Nyquist theorem. It can also be considered that the presence of a residual, non-constant contribution from the background can never be totally ruled out. This uncertain disturbance can however be expected to be small after subtraction of the estimated background and to mostly affect the radial profiles at large nucleocentric distance. In contrast, uncertainties concerning the centering of the image of the coma are more likely to disturb the radial profile at small nucleocentric distance. Along the same lines, the cumulated effects of flat-field, radial and azimuthal averaging and velocity terms in the outflow can become important at large nucleocentric distance. Both the fitting of the Haser model and the numerical inverse Abel transform will incorporate these effects as if they were physically meaningful contributions, which can somewhat bias the radial profile at large nucleocentric distance.

Interestingly enough, the emission rate plotted in log-log scales presents a change of slope near $r = L_p$. This change of slope is less visible in the observed flux, although one can make it out a posteriori, after having first noticed it in the emission rate profile. Comet 103P/ Hartley 2 was located at a heliocentric distance of 1.07 au at the time of the observation. The reference characteristic lengths from A'Hearn et al. (1995) for CN are $L_d^* = 2.1\times10^5$ km and $L_p^* = 1.3\times10^4$ km at 1 ua, to be scaled by the square of the heliocentric distance giving L_p = 14900 km and L_d = 240000 km. The fitted L_p is comparable with the standard reference value, but L_d is quite different. Determining a scale length much longer than the radius range over which the data are available is however a difficult task, and it is not sure it is always possible, especially when noise affects the data (and has to be taken into account for the fit, as it was done here) and when the model does not perfectly match the observation (as it can often be expected from a Haser model).

It must be noted here that, when a model is adjusted using a least squares fit with weighting by the inverse of the variances, it is expected that the differences between the data and the fitted curve would be distributed along a Gaussian centered on the fitted curve. It is not exactly the case here: the data are not distributed exactly symmetrically with respect to the fitted flux because the regularization modifies the concept of optimum (the algorithm does not strictly minimize the classical χ^2) and produces a smoother result.

Emission of CN at 387 nm from comet C/2012 F6 Lemmon was also observed with ESO-TRAPPIST on February 17, 2013. Comet Lemmon was a very active naked eye comet that reached mag 5 at perihelion, on March 24, 2013. It is a dynamically old, long-period comet following a highly eccentric and inclined orbit. **Figure 10** shows the inversion of its profile. Again, the observed flux is correctly fitted by the method. The emission rate is affected with minor uncertainties only. However, the emission rate does not seem to make sense near the comet’s nucleus, although the observed flux is perfectly fitted. This is due to the fact that flux measurements near the nucleus are somewhat more uncertain than the low level of noise affecting it may let suppose. For example, accurate centering (identification of the exact location of the nucleus in TRAPPIST images) is a source of uncertainties, as well as the subtraction of possible contributions from dust, especially if we take into account that the dust profile was obtained separately from the CN profile, so that the centering of both observations of the comet may not perfectly match. The inverted profile offers here a means to diagnose a feature that might have remained unnoticed in the radial profile of the flux: either the first points of the profile are erroneous, or this is a real feature of the radial profile of the emission rate. Indeed, the first points of the profile near the nucleus must be considered with care because, in terms of the Nyquist theorem, information can hardly be obtained at a resolution better than 2-4 pixels. Indeed, the limitations considered in the analysis of the Hartley 2 data also hold in this case, so that conclusions reached regarding the extremes of the radial profile must be considered with care. For a comet such as C/2012 F6 Lemmon, which was very productive, a low emission rate profile near the nucleus could be the signature of significant absorption of the solar UV radiation. Validation of this hypothesis would need a thorough verification, which is beyond the scope of the present study. The emission rate can again be represented using a Haser model using least squares fitting, giving characteristic lengths $L_p = 3.11\times10^4$ km and $L_d = 2.35\times10^5$ km. This last length is comparable (up to a factor ~2) with the radial range of the data used to determine it and should be considered with caution. F6 Lemmon was located at a heliocentric distance $r_H = 1.01$ au and had a heliocentric radial velocity $\dot{r}_H = -21.9$ km/s at the time of the observation, giving $g_{CN} = 4.41\times10^{-13}$ erg s^{-1} molecule^{-1}, from which we estimate the effective production rate $Q_{HCN} = 8.88\times10^{26}$ molecule s^{-1}. The reference characteristic lengths of CN are $L_d^* = 2.1 \text{ x } 10^5$ km and $L_p^* = 1.3\times10^4$ km at 1 ua, to be scaled by the square of the heliocentric distance giving $L_p = 1.33\times10^4$ km and $L_d = 2.14\times10^5$ km. The fitted L_d value is comparable with the standard reference value, while the shorter L_p values differ by a gross factor of 2. By fitting a Haser model directly on the observed flux, we find $L_p^{(F)} = 3.8\times10^4$ km, $L_d^{(F)} = 1.77\times10^5$ km and $Q_{HCN}^{(F)} = 1.02\times10^{27}$ particles s^{-1}. These characteristic lengths differ again from those obtained using the emission rate profile. Again, adding a small offset (2.8×10^{-4} erg cm^{-2} s^{-1} sr^{-1}) to the flux can bring the fitted lengths closer to those of the emission rate profile, suggesting again the effect of the sensitivity to the sky background. The background subtracted from this TRAPPIST image did however correspond to ~2×10^{-5} erg cm^{-2} s^{-1} sr^{-1}, an order of magnitude lower than the needed offset, so that the explanation for the difference must be searched for elsewhere. A possible explanation could be that the flat flux found near the comet nucleus implies that the emission rate must, surprisingly, increase with the nucleo-centric distance in the first layers of the coma. A Haser model cannot reproduce such an emission rate. However, the flat flux is rather smooth and non-increasing, which is easier to model using a Haser profile. The inadequacy of the Haser model to represent the coma of comet F6/Lemmon could then be the origin of the discrepancy. It must also be kept in mind that the anomalous, increasing emission rate is found within a radius corresponding to only ~2 pixels of observation, and the inferred variation may thus just be an artifact due to the insufficient resolution of the observation, uncertainties in the centering and the background subtraction, etc. As already discussed above, the analysis of the data obtained near the comet nucleus is not straightforward.

Figure 11 shows the emissions of CN molecules at 387 nm and of C_2 at 514.1 nm from the comet C/2013 A1 Siding Spring on November 11, 2014 observed again with the TRAPPIST telescope. Comet Siding Spring was discovered at 7.2 au from the Sun on January 3, 2013 and it was soon predicted to have a close encounter with planet Mars on October 19, 2014. The comet has been extensively observed from the ground and from orbiters around Mars at the time of the encounter. It underwent an outburst that increased the gas production fivefold within a few days, less than two weeks after its perihelion passage on October 25, 2014 (Opitom et al., 2016). The C_2 514.1 nm emission belongs to the (0-0) band of the Swan transition system d $^3\Pi_g$ – X $^1\Sigma_g^+$. Molecular C_2 can be produced by photodissociation of C_2H_4, C_3H_6 and possibly C_2H_6 in cometary atmospheres (Weiler, 2012; Helbert et al., 2005), and the 514.1 nm emission is fed by absorption of the solar light and is due to (at least at large nucleo-centric distance) the complex fluorescent equilibrium that includes the transitions A $^1\Pi_u$ – X $^1\Sigma_g^+$, b $^3\Sigma_g^-$ – a $^3\Pi_u$, d $^3\Pi_g$ – a $^3\Pi_u$, d $^3\Pi_g$ – c $^3\Sigma_u^+$, a $^3\Pi_u$ – X $^1\Sigma_g^+$, and c $^3\Sigma_u^+$ – X $^1\Sigma_g^+$

(Rousselot et al., 2000). The comet was located at a heliocentric distance of 1.43 au and had a heliocentric radial velocity $\dot{r}_H$ = 5.03 km/s. The fluorescence g-factors obtained from Schleicher (2010) for CN and A'Hearn et al. (1982) for C_2 under these conditions are g_{CN} = g_{C2} = 2.2 x 10^{-13} erg s^{-1} $\mathrm{molecule}^{-1}$ (both values are incidentally equal). The radial profiles of the observed fluxes and of the emission rates deduced after Abel inversion are shown in **Figure 11**. Again, we used three times less u_k elements than the number of bins in the observed profiles plus a few bins beyond the last observed point, and we applied the Tikhonov regularization, so that the fitted flux of the C_2 emission is smoother than the observed flux. Its uncertainties remain small, though. The inverted radial profile for the emission rate appears to be overestimated. Indeed, the small "bump" that appears in the flux near r = 5000 km does not seem to be real. This feature does however not seem to be dramatic in the l.o.s.-integrated flux, but it influences the radial profile of the emission rate. Accordingly, the inverted profile turns out to be a useful tool to diagnose the quality of the flux profile or perhaps a real phenomenon: indeed, this feature could possibly be attributed to an underestimate of the contribution from the dust, which was subtracted, and that seems to become less important beyond ~10000 km. Moreover the second pixel of the profile corresponds to r = ~3000 km only, and the issue raised above concerning the Nyquist frequency holds here again, re-emphasizing that it is difficult to draw definite conclusions from observations obtained close to the nucleus. The Haser model fitted to the radial profile of the C_2 514.1 nm emission rate was obtained neglecting the contribution of the points below 10000 km. We find nearly identical values for L_p and L_d : L_p = 34273 km and L_d = 34302 km while the effective production rate of the C_2 parents is found to be Q_{C2Hn} = 4.75×10^{26} particles s^{-1}. The lengths are given with such a high accuracy because, having L_p exactly equal to L_d would be physically inconsistent. The limit of the Haser model (**equation 3**) for L_d tending to L_p is proportional to 1/r, which cannot be integrated over $\mathbb{R}^3$. In addition, the Abel transform (**equation 4**) of such a profile tends to infinity, whatever the value of r_0. Finding nearly equal values for L_p and L_d may possibly indicate that there is outgassing from the dust grains. Combi and Fink (1997) explain that C_2 radial profiles are usually flatter than would be expected for the photodissociation of a single parent molecule, and can then be more easily reproduced with a Haser model that has two almost equal scale lengths. Interestingly, the radial profile of the emission rate of CN has L_p = 37646 km and L_d = 37688 km. CN would thus also have nearly equal characteristic lengths, which are above all nearly identical to those of C_2, thus corroborating the hypothesis of outgassing from grains. However, as we will show in the next paragraph, such a conclusion cannot be drawn in the case of Siding Spring. The effective production rate derived from the CN emission rate profile is Q_{HCN} = 4.20×10^{26} particles s^{-1}.

There are oscillations that can be seen at large nucleo-centric distance (above ~1.5×10^5 km) in the radial profile of the emission rate of C_2 and, to a lesser extent, in the emission rate profile of CN where a change of slope appears (in the log-log plot of **Figure 11b**). These signatures require particular attention. Comet Siding Spring is known to have produced an outburst shortly before these data were obtained (Opitom et al., 2016). Inverse Abel transform is particularly adapted to retrieve the radial profile of the emission rate in this dynamic case, as standard models generally assume steady state. Indeed, both the C_2

514.1 nm and the CN 387 nm fluxes show a smooth change of slope around 10^5 km. The radial profile of the CN 387 nm emission rate clearly shows a slope breaking at 1.5×10^5 km. A similar breaking is also seen at the same place in the radial profile of the C_2 514.1 nm emission (see **Figure 12**), especially comparing the emission rate obtained by Abel inversion and the Haser model fitted to the emission rate at nucleocentric distance larger than 1.5×10^5 km. Note that C_2 is known to have a shorter lifetime than CN, leading to a smaller characteristic length (A'Haern et al., 1995). This leads to a faster radial decrease of the C_2 emission rate compared with CN, as it is easily seen in **Figure 12**, and the signature of the outburst is then harder to detect in the C_2 profile. The oscillation that appears in the C_2 emission and peaks at 3×10^5 km may be due to the poorer quality of the observed flux near that nucleo-centric distance, and it is hard to draw conclusions about it. It remains that both the CN and C_2 emission rate profiles show a clear signature of the outburst, seen as a breaking of both profiles near 1.5×10^5 km. The information is of course present in the radial profiles of the observed flux, but the l.o.s. integration smoothens the features present in the emission rate, and it is harder to determine where the junction between the pre- and post-outburst coma is located. The presence of the outburst also casts another light on the characteristic lengths deduced from the fitting of a Haser profile over the emission rate: the observed coma does not comply with the hypothesis of the Haser model, that assumes a fairly constant production rate, and it is hazardous to draw any conclusion over the outgassing mechanisms at play in the coma at that time (although outgassing from grains could make sense right after the outburst, if it were related with an explosive release of matter). In contrast, the numerical inverse Abel transform does not rely on any assumption regarding the functional shape of the radial profile and it can thus account for possible dynamic variations of the production rate of the nucleus and for a possible extended source.

5. DISCUSSION

We developed an inverse Abel transform method with Tikhonov regularization that specifically accounts for the properties of cometary atmospheres. We used triangular elements matching the density profiles of chemically inert species. However, using more elaborate elements that closely resemble the Haser model for daughter species might have been more appropriate. We had to make a tradeoff between adequacy of the elements and computational efficiency. First of all, the Abel transform of these alternative elements would have been more difficult to compute. Secondly, the least squares fitting on which the method relies would have become non-linear. The impact of more sophisticated triangular elements is difficult to assess. Our theoretical tests tend to show that the elements used in this study have properties that are adequate for the processing of cometary observations.

The Abel inversion method calls upon the hypothesis of spherical symmetry of the coma. This assumption is probably never strictly fulfilled, although one may expect that it is valid far from the nucleus. It is difficult to appreciate how large deviations from spherical symmetry can possibly be. Alternatively, one could develop a model under the hypothesis of axial symmetry about the rotation axis of the comet and directly use 2D imaging of the coma to perform an inversion. We conducted a preliminary analysis that suggests such a method could probably be developed and applied when the orientation of the rotation axis is known with sufficient accuracy. However, further developments are required to fully explore the potential of such a method. One may also dream of a method that would produce a 3D tomographic inversion of cometary observation. Such a method would rely on the (inverse) Radon transform which is extensively used in medical imagery, so that an impressive know-how exists about that topic. Such an inversion would however require observations under all possible look directions (i.e. from vintage points distributed in the 4π steradians around the comet). That kind of observation will not be available on a regular basis in a foreseeable future, if it ever becomes available.

Application to real cometary observation showed to be efficient in the sense that realistic emission rate profiles could be retrieved from the Abel inversion of the observed flux of radiation. However, comparison between the properties of Haser models fitted over the emission profile and over the observed flux reveals differences in the inferred scale lengths. It is possible to reconcile the numbers by applying a small offset to the observed flux data prior to fitting a Haser model to them, given that the inverse Abel transform applied to noisy data is only weakly sensitive to an offset (which may be related to inaccuracies in the estimate of the sky background). This ad hoc cure may however seem somewhat artificial as it introduces an additional degree of freedom to the problem to reach internal consistency. The independence of the theoretical inverse Abel transform over any applied offset gives nevertheless confidence in the offset explanation of the apparent discrepancies, although an imperfection of the data reduction technique can never be totally ruled out.

The inverse Abel transform has proven to be a powerful tool when applied to real observations. It allows an easy diagnosis of the properties of the observation. We were able to identify a possible anomaly in the dust contribution subtracted from the observation of comet A1/ Siding Spring. We were also able to identify a signature in the emission rate profile of comet F6/ Lemmon that may be attributed either to an inaccuracy in the data (possibly due to a problem with the exact identification of the location of the comet nucleus in the TRAPPIST images for example) or that may have a physical explanation, such as significant absorption of the solar UV light by the material of the coma, especially considering that comet F6/ Lemmon was very productive. Whatever the explanation will be, those signatures would have remained unnoticed in the flux profile, while they are patent in the emission rate profile. The analysis of an image of an outburst of comet A1/ Siding Spring with our new method may provide original insight: the separation between the pre- and post-outburst coma could be easily identified in both emission rate profiles from molecules CN and C_2. If consecutive observations can be obtained over timescales of a few hours up to a few days, it would be possible to track the location of that junction versus time, to estimate the velocity at which it propagates in the coma, and to determine at what time the outburst actually takes place at the nucleus.

A further consistency check of the fitted parameters can be performed considering the total content of daughter species in the coma. For a Haser density profile with production rate Q and expansion velocity v, the number of particles inside a sphere of radius R centered on the nucleus is

$$N(R) = \frac{Q}{v}\frac{L_d}{L_d - L_p}\left(L_p \exp\left(-\frac{R}{L_p}\right) - L_d \exp\left(-\frac{R}{L_d}\right) + L_d - L_p\right) \tag{39}$$

and the fraction of the total number of particles inside of that sphere is obtained by the ratio $\beta = N(R) / (Q\, L_d/v)$. When the coma is observed over range R of radii, $N(R)$ can also be directly obtained from the observation by integrating the flux (given per steradian) over the observed disc, if the fluorescence g-factor is known:

$$N(R) = 2\pi \int_0^R dr_0\, r_0\, F(r_0)\ \frac{4\pi}{g}. \tag{40}$$

In the case of comet 103P/Hartley2, the Haser parameters fitted over the emission rate give a coma content of 1.908×10^{30} CN molecules, 73% of which are contained inside a sphere of radius given by the maximum radius of the observation. The content of that sphere calculated from equation (40) is 1.372×10^{30} particles which, when divided by 0.73, gives an estimated total coma content of 1.88×10^{30} molecules, in excellent agreement with the value derived from the fitted Haser model. The results provided by the different methods are thus consistent, and in particular, corroborate the assumption of a Haser density profile, at least as far as the global properties of the coma are considered. We reached similar conclusions with the F6/Lemmon observations: both estimates of the CN coma content agree within 0.5%. On the opposite, in the case of comet Siding Spring, both methods for estimating the coma content differ by ~11% using the C_2 observation and ~24% using the CN observation, which indicates that a Haser model cannot be used to represent the density profiles of a coma shortly after an outburst.

The method does not make any assumption about the detailed nature of the observation (except that it is a cometary observation). It could thus be applied to any emission, to the study of dust, and it could be adapted to the study of absorption phenomena, such as star occultation for example, in which the material of the coma or of a planetary atmosphere absorbs the light emitted by stars depending on the amount of gas present along the total line of sight. In the case of planetary atmospheres, this technique can be used by measuring the absorption of sun light aboard an orbiting spacecraft. The method thus appears to be a promising tool capable of simplifying the analysis of various cometary observations.

More sophisticated representations of the density profile of the coma might also be included in the analysis of the emission rate retrieved after Abel inversion. The vectorial model of the coma offers a more detailed description of the photochemical processes responsible for the production of the daughter species, and thus of the destruction of the mother species. As explained by Festou (1981), inclusion of the vectorial effects has, as a major consequence, that molecules produced at a given location can end up at another location which is not necessarily located downstream of the production location. Daughter molecules are produced isotropically in a reference frame moving with the expanding gas of the coma. All the points of the coma are thus coupled by diffusive transport. In other words, the isotropic production of daughter molecules leads to a kind of smoothing of the composition of the coma. One can thus naturally expect that scale lengths fitted over the observed coma should be somewhat longer than those we would compute using the photochemical reaction constants, given with an appropriate accuracy from laboratory measurements, using a prescribed profile for the major constituents and neglecting molecular diffusion. One would furthermore expect that these ad hoc fitted lengths would be influenced by the value of the collisional mean free path, which constrains the diffusive transport of the daughter molecules. The numerical Abel inversion method transforms line-of-sight integrated quantities into local quantities. It can, unfortunately, not be used to identify the effect of molecular diffusion without additional processing. The first and second derivatives of the emission rate as a function of the radial distance could possibly provide quantitative information on the effect of diffusive smoothing in relation with the collisional mean free path, something that could probably not easily be done directly using the radial profile of the flux alone. So far neither the feasibility nor the validity of this idea have been tested. The practical implementation of such an analysis would need a reasonable estimate of the collision cross sections required to evaluate the gas kinetic, and validation should rely on detailed modelling of the molecular diffusion inside of the expanding coma (e.g., with a Monte Carlo method or an average random walk technique such as the one developed by Combi and Delsemme (1980a,b)). This idea could be tested independently of the inversion technique developed here.

6. CONCLUSIONS

1. We have developed a numerical inverse Abel transform specifically adapted to cometary atmospheres. Its efficiency is considerably improved in combination with a Tikhonov regularization. It allows the usage of standard error propagation techniques to estimate the uncertainties that affect the local emission rates derived from the observed flux of radiation.

2. The emission rates calculated with our inverse Abel transform are only weakly sensitive to a constant offset that might result from an inaccurate subtraction of the sky background with real-world data.

3. We applied our inversion technique to a restricted set of observations of comets and found that it effectively yields realistic emission rate. The emission rate profiles allow an easier diagnostic of the characteristics of the observation, such as an erroneous estimate of the dust subtraction or the identification of a signature possibly attributable to significant UV absorption by the coma.

4. When we applied our method to an outburst case, we were able to clearly identify the separation between the pre- and post-outburst parts of the coma, which further illustrates its efficiency.

APPENDIX 1

In this section, we present the analytical results needed to use triangular elements $v_k = t_k/(r-a)^m$. Such elements could be useful to realize the inverse Abel transform of planetary observation. The value of the parameter a can be adjusted to make the elements more appropriate for the properties of the observed atmosphere. The computation of the Abel transform of elements v_k is necessary to realize the inversion of an observed profile and requires the computation of indefinite integrals of the form

$$\int dr \, \frac{r}{\sqrt{r^2 - r_0^2}} \, t_k(r) \frac{1}{(r-a)^m}, \qquad 0 < a < r_{0.} \tag{A1.1}$$

These can always be reduced to a linear combination of indefinite integrals of the form

$$W_m = \int dr \, \frac{1}{\sqrt{r^2 - r_0^2}} \frac{1}{(r-a)^m} \tag{A1.2}$$

completed with the first elements of the suite of integrals I_n given by equations (6) and (7) when m is lower than 3. These integrals satisfy a recurrence relation and are also related by a simple derivative with respect to the parameter a:

$$\begin{aligned}
&\frac{\partial W_m}{\partial a} = m \, W_{m+1} \quad (m > 0) \\
&m \, (r_0^2 - a^2) \, W_{m+1} = \frac{\sqrt{r^2 - r_0^2}}{(r-a)^m} + (2m-1) a \, W_m + (m-1) W_{m-1} \\
&W_0 = \operatorname{arcosh}\left(\frac{r}{r_0}\right) = \ln\left(\frac{r}{r_0} + \sqrt{\frac{r^2}{r_0^2} - 1}\right) \\
&W_1 = \frac{1}{\sqrt{r_0^2 - a^2}} \operatorname{arctg}\left(\frac{ar - r_0^2}{\sqrt{(r_0^2 - a^2)(r^2 - r_0^2)}}\right) \\
&W_2 = \frac{\partial W_1}{\partial a} = \frac{\sqrt{r^2 - r_0^2}}{(r_0^2 - a^2)(r-a)} + \frac{a}{\sqrt{(r_0^2 - a^2)^3}} \operatorname{arctg}\left(\frac{ar - r_0^2}{\sqrt{(r_0^2 - a^2)(r^2 - r_0^2)}}\right).
\end{aligned} \tag{A1.3}$$

The recurrence relation can be obtained by multiplying and dividing the integrant by a in (A1.2), then replacing the factor a at the numerator by a–r+r in order to make appear $W_{m\text{-}1}$ and a second indefinite integral that can be reduced by an integration by parts, leading to

$$a \, W_m = -W_{m-1} + \frac{\sqrt{r^2 - r_0^2}}{(r-a)^m} + m \int dr \, \frac{r^2 - a^2 + a^2 - r_0^2}{\sqrt{r^2 - r_0^2}} \frac{1}{(r-a)^{m+1}}, \tag{A1.4}$$

where we have already introduced $-a^2+a^2$ at the numerator of the integrand. The indefinite integral in (A1.4) can now easily be expressed as a combination of W_m by noting that $r^2-a^2 = (r-a)(r+a)$. The factor (r–a) can be cancelled with one and we finally retrieve the recurrence relation (A1.3). W_0 can be directly derived from (A1.2). W_1 is more difficult to obtain, as it cannot be derived from W_0 by simple derivation with respect to a. To obtain the expression for W_1, we first let $x = r/r_0$ and, accordingly, $dx = dr/r_0$ (we also denote $b = a/r_0$). We then apply the substitution $x = 1/\cos(u)$, $dx = \mathrm{tg}(u)/\cos(u)\, du$, which leads to

$$W_1 = \frac{1}{r_0}\int du\ \frac{1}{1-b\cos(u)} \qquad (b = \frac{a}{r_0}) \tag{A1.5}$$

With the classical substitution s = tg(u/2), i.e., cos(u) = $(1-s^2)/(1+s^2)$, sin(u) = $2s/(1+s^2)$, du = $2/(1+s^2)\, ds$ we get

$$W_1 = \frac{1}{r_0}\int ds\ \frac{2}{1-b+(1+\mathrm{b})\,\mathrm{s}^2} \tag{A1.6}$$

which reduces to an arctangent. After back-substitution of the variable changes, one finds (up to an additive constant):

$$W_1 = \frac{1}{r_0}\ \frac{2}{\sqrt{1-b^2}}\mathrm{arctg}\left(\frac{bx-1+x-b}{\sqrt{(1-b^2)(x^2-1)}}\right). \tag{A1.7}$$

Noting that 2 arctg(y) = arctg($2y/(1-y^2)$)+π and arctg(y)+arctg($1/y$) = sgn(y) π, and substituting $x = r/r_0$ and $b = a/r_0$, we finally get the expression from (A1.3)

$$W_1 = \frac{1}{\sqrt{r_0^2-a^2}}\mathrm{arctg}\left(\frac{ar-r_0^2}{\sqrt{(r_0^2-a^2)(r^2-r_0^2)}}\right) \tag{A1.8}$$

which is defined up to an additive constant. Derivation with respect to a immediately gives W_2 and the recurrence can be started. Care must however be taken when using that recurrence. The numerical tests that we performed suggest that it is not always stable. The relations given in equation (A1.3) can nevertheless be used to derive analytical expressions of the W_m and thus of any integral of the form of expression (A1.1). Based upon these results, the inversion method developed above can be adapted for triangular elements of the form

$$v_k = t_k\ \frac{1}{(r-a)^m}, \tag{A1.9}$$

which have an Abel transform $V_k(r_0)$ for any $r_0 > a$ (all of which can now be calculated from the W_0, W_1 and W_2 above because of the linearity of the Abel transform), to be used instead of T_k in the developments of equations (13), (16) and (19). In the case of planetary atmospheres, choosing a of the order of the radius of the planet could be appropriate to build triangular elements adapted to the observed atmosphere.

APPENDIX 2.

In this section, we provide the detailed developments needed to analytically compute the line-of-sight integration of a Haser model for mother and daughter species.

All integrals appearing in the l.o.s. integration of a Haser model for parent and daughter species can always be reduced, after the substitution $x = r/r_0$, to integrals of the form:

$$P = \int_1^\infty dx\ \frac{\exp(-q\,x)}{x\sqrt{x^2-1}}. \tag{A2.1}$$

We first derive P with respect to q:

$$\frac{dP}{dq} = -\int_1^\infty dx\ \frac{\exp(-q\,x)}{\sqrt{x^2-1}} = -\int_0^\infty dt\,\exp(-q\cosh(t)) \tag{A2.2}$$

where we made the variable change $x = \cosh(t)$, $t = \operatorname{arcosh}(x)$, $dt = dx\,/\,(x^2-1)^{1/2}$. This integral can be easily computed with the well-known formula for the modified Bessel functions of the second kind, $\underline{B_K}(n,z)$ (Abramowitz and Stegun, 1972):

$$B_K(n,z) = \int_0^\infty dt\,\exp\big(-z\,cosh(t)\big)\cosh(n\,t) \tag{A2.3}$$

to be applied with $n = 0$, so that

$$\frac{dP}{dq} = -B_K(0,q), \tag{A2.4}$$

a result already given by Haser (1957).

Now, we must compute the indefinite integral of $B_K(0,q)$ to retrieve P up to an additive constant. We use the following formula, from Olver et al. (2010), and which can also be found in the digital version of the NIST handbook of mathematical functions (the Digital Library of Mathematical Functions, DLMF) as equation 10.43.2:

$$\begin{aligned}\int dz\,z^n\,e^{in\pi}B_K(n,z)\\ &= \sqrt{\pi}\,2^{n-1}\Gamma\left(n+\tfrac{1}{2}\right)z\,\Big(e^{in\pi}B_K(n,z)\,S_L(n-1,z)\\ &- e^{i(n-1)\pi}B_K(n-1,z)\,S_L(n,z)\Big)\ +c,\end{aligned} \tag{A2.5}$$

where $S_L(n,z)$ represents the modified Struve function (also called Struve-L), which can be easily computed using a fast-converging series expansion (Abramowitz and Stegun, 1972):

$$S_L(n,z) = \left(\tfrac{1}{2}z\right)^{n+1}\sum_{k=0}^{\infty}\frac{\left(\frac{1}{2}z\right)^{2k}}{\Gamma\big(k+\frac{3}{2}\big)\ \Gamma(k+n+\frac{3}{2})} \tag{A2.6}$$

If we let $n = 0$ in equation (A2.5), the gamma function can be evaluated as $\Gamma(1/2) = \pi^{1/2}$ and expression (A2.5) reduces to

$$\int \mathrm{dz}\,B_K(0,\mathrm{z}) = \frac{\pi}{2}\,z\,\big(B_K(0,z)\,S_L(-1,z) + B_K(-1,z)\,S_L(0,z)\big)\ +c, \tag{A2.7}$$

so that we can write

$$P = -\tfrac{\pi}{2}\,q\,\big(B_K(0,q)\,S_L(-1,q) + B_K(-1,q)\,S_L(0,q)\big) + C. \tag{A2.8}$$

We determine the integration constant C by noting that, when q becomes infinitely large, the integrant in (A2.1) becomes zero for any $x \in\ ]1,\infty[$, so that P tends to 0 as well. The limit of equation (A2.8) for q tending to infinity is computed using the asymptotic developments given by Abramowitz and Stegun (1972). For large values of z, noting $B_I(n,z)$ the modified Bessel functions of the first kind, we have

$$
\begin{aligned}
&B_K(n,z) \sim \sqrt{\frac{\pi}{2\,z}}\, e^{-z}\left(1 - \frac{4\,n^2 - 1}{8\,z} + \cdots\right)\\
&S_L(n,z) \sim B_I(-n,z) + \frac{1}{\pi}\sum_{k=0}^{\infty} \frac{(-1)^{k+1}\Gamma\left(k+\frac{1}{2}\right)}{\Gamma\left(n+\frac{1}{2}-k\right)\left(\frac{z}{2}\right)^{2k+n+1}}\\
&B_I(n,z) \sim \sqrt{\frac{1}{2\pi\,z}}\, e^{+z}\left(1 - \frac{4\,n^2 - 1}{8\,z} + \cdots\right)
\end{aligned}
\qquad \text{(A2.9)}
$$

with $|\arg(z)| < 3\pi/2$ when z is complex. For very large values of z, the exponential term in the expression of $B_I(n,z)$ will largely dominate the series that appears in the asymptotic development of $S_L(n,z)$, so that we can immediately write that

$$
\lim_{z\to\infty} z\, B_K(0,z)\, S_L(-1,z) = \lim_{z\to\infty} z\, B_K(-1,z)\, S_L(0,z) = \tfrac{1}{2} \qquad \text{(A2.10)}
$$

It follows that, in (A2.8), C = $\pi/2$ and we have

$$
P = \int_1^{\infty} dx\, \frac{\exp(-q\,x)}{x\sqrt{x^2-1}} = \frac{\pi}{2}\left(1 - q\left(B_K(0,q)\, S_L(-1,q) + B_K(-1,q)\, S_L(0,q)\right)\right) \qquad \text{(A2.11)}
$$

It is always possible to compute P numerically, although this integration must be carried out with extreme care as the integrant tends to infinity when x approaches 1. The analytical expression (A2.11) uses special functions that can be rapidly computed with modern computers, with an accuracy that will approach the machine precision. The advantage of (A2.11) is thus twofold: it offers a better accuracy and it is faster than numerical integration, which is important when P must be evaluated a large number of times, as it is the case in least squares fit procedures. The benefit can be expected to be even larger when handling a more sophisticated model using similar analytic expressions such as the three-generation Haser-like model (Combi et al., 2004).

For the sake of completeness, we define a suite of integrals of the form

$$
D_n = \int_1^{\infty} \frac{exp(-qx)}{x^n\sqrt{x^2-1}}\, dx\ . \qquad \text{(A2.12)}
$$

Proceeding by parts, it is easily shown that these integrals satisfy a recurrence of third order (letting $U=exp(-q\,x)/x^{n+1}$ and $dV=x/(x^2-1)^{1/2}\,dx$):

$$
D_{n+2} = \frac{q}{n+1}\, D_{n-1} + \frac{n}{n+1} D_n - \frac{q}{n+1} D_{n+1}\ . \qquad \text{(A2.13)}
$$

Evaluation of any three of the D_n ($n \geq 0$) suffices to start the recurrence, and successive D_n's are also related by a derivative versus parameter q. We already know $D_0 = B_K(0,q)$ (equation

A2.4) and $D_1 = P(q)$ (equation A2.11). Integral D_2 is evaluated proceeding by parts, letting $U = exp(-qx)$ and $dV=dx/(x^2 (x^2-1)^{1/2})$ to find

$$D_2 = q \int_1^{\infty} \frac{x\ exp(-qx)}{\sqrt{x^2-1}}\ dx - q \int_1^{\infty} \frac{exp(-qx)}{x\sqrt{x^2-1}}\ dx \qquad \text{(A2.14)}$$

The first of these integrals is computed using the change of variable $x = cosh(t)$, $t = arcosh(x)$, $dt = dx / (x^2-1)^{1/2}$ and equation (A2.3), while the second integral is given in equation (A2.11) so that

$$D_2 = q\ B_K(1, q) - q\ P(q)\ . \qquad \text{(A2.15)}$$

Recurrence (A2.13) can then be started and all the D_n's can be computed. These results can be used to compute indefinite integrals of $D_n(q)$ and in particular the analytical primitive of $P(q)$, an unexpected result. Because $-D_{n-1}$ is the derivative of D_n versus q, the recurrence (A2.13) can be transformed in a set of differential equations that admit D_n as solutions. A similar remark can be made concerning recurrence (A1.3).

Acknowledgements.

D.V. Bisikalo and V.I. Shematovich were supported by RSCF 14-12-01048. B.Hubert, C. Opitom, D. Hutsemekers, G. Munhoven, J. Manfroid and E. Jehin are supported by the Belgian Fund for Scientific Research FRS-FNRS.

REFERENCES

Abramowitz, M., and I. Stegun, 1972. Handbook of Mathematical Functions with formulas, graphs and mathematical tables. Dover Publications, New York.

Ahearn, M. F. 1982. Spectrophotometry of comets at optical wavelengths, in IAU Colloq. 61: Comet Discoveries, Statistics, and Observational Selection, edited by L. L. Wilkening, pp. 433–460.

A'Hearn, M. F., R. C. Millis, D. O. Schleicher, D. J. Osip, and P. V. Birch, 1995. The ensemble properties of comets: Results from narrowband photometry of 85 comets, 1976-1992. Icarus, 118, 223–270, doi: 10.1006/icar.1995.1190.

A'Hearn, M. F., et al., 2011, EPOXI at Comet Hartley 2, Science, 332, 1396, doi: 10.1126/science.1204054

Arpigny C., Detailed study of the CN violet (0, 0) band in cometary spectra, *Ann. D'Ap.* **27**, 1964, 393 – 405.

Bhardwaj, A., and S. Raghuram, 2012. A Coupled Chemistry-emission Model for Atomic Oxygen Green and Red-doublet Emissions in the Comet C/1996 B2 Hyakutake. ApJ. , 748, 13, doi: 10.1088/0004-637X/748/1/13.

Bisikalo, D. V., V. I. Shematovich, J.-C. Gérard, E. Jehin, A. Decock, D. Hutsemékers, J. Manfroid, and B. Hubert, 2015. Monte Carlo Simulation of Metastable Oxygen Photochemistry in Cometary Atmospheres, ApJ. , 798, 21, doi: 10.1088/0004-637X/798/1/21.

Biver, N., et al., 1999. Spectroscopic Monitoring of Comet C/1996 B2 (Hyakutake) with the JCMT and IRAM Radio Telescopes. Astron. J., 118, 1850–1872, doi: 10.1086/301033.

Bracewell, R., 1999. The Fourier Transform and Its Applications, 3 ed., McGraw-Hill, New York.

Combi, M. R. and A.H. Delsemme, 1980a. Neutral cometary atmospheres. I - an average random walk model for photodissociation in comets, ApJ, 237, 633-640, doi: 10.1086/157909.

Combi, M. R. and A.H. Delsemme, 1980b. Neutral cometary atmospheres. II - The production of CN in comets, ApJ, 237, 641-645, doi: 10.1086/157910.

Combi, M. R. (1996), Time-Dependent Gas Kinetics in Tenuous Planetary Atmospheres: The Cometary Coma, Icarus , 123, 207–226, doi: 10.1006/icar.1996.0150.

Combi, M. R., and U. Fink, 1997. A Critical Study of Molecular Photodissociation and CHON Grain Sources for Cometary C2. Astrophys. J. , 484, 879–890.

Combi, M. R., W. M. Harris, and W. H. Smyth, 2004. Gas dynamics and kinetics in the cometary coma: Theory and observations, in *Comets II*, University of Arizona Press, ed. M. Festou, H. U. Keller, & H. A. Weave, pp. 523-552.

Cox, C., A. Saglam, J.-C. Gérard, J.-L. Bertaux, F. González-Galindo, F. Leblanc, and A. Reberac, 2008. Distribution of the ultraviolet nitric oxide Martian night airglow: Observations from Mars Express and comparisons with a one-dimensional model. J. Geophys. Res. , 113, E08012, doi: 10.1029/2007JE003037.

Ehrenfreund P., and S.B. Charnley, Organic molecules in the ISM, comets and meteorites: A voyage from dark clouds to the early Earth, *ARA&A* **38**, 2000, 427 - 483, doi: 10.1146/annurev.astro.38.1.427

Farnham, T. L., D. G. Schleicher, and M. F. A'Hearn, 2000. The HB Narrowband Comet Filters: Standard Stars and Calibrations. Icarus, 147, 180–204, doi: 10.1006/icar.2000.6420.

Festou, M. C., 1981. The density distribution of neutral compounds in cometary atmospheres. I - Models and equations, A&A, 95, 69-79.

Fray, N., Y. Bénilan, H. Cottin, M.-C. Gazeau, and J. Crovisier (2005), The origin of the CN radical in comets: A review from observations and models. Planet. Space. Sci., 53, 1243–1262, doi: 10.1016/j.pss.2005.06.005.

Haser, L., 1957. Distribution d'intensité dans la tête d'une comète. Bulletin de la Société Royale des Sciences de Liège, 43, 740–750.

Helbert, J., H. Rauer, D. C. Boice, and W. F. Huebner, 2005. The chemistry of C2 and C3 in the coma of Comet C/1995 O1 (Hale-Bopp) at heliocentric distances rh 2.9 AU. A&A., 442, 1107–1120, doi: 10.1051/0004-6361:20041571.

Jehin, E., M. Gillon, D. Queloz, P. Magain, J. Manfroid, V. Chantry, M. Lendl, D. Hutsemékers, and S. Udry, 2011. TRAPPIST: TRAnsiting Planets and PlanetesImals Small Telescope. The Messenger, 145, 2–6.

Olver, F. W., D. W. Lozier, R. F. Boisvert, and C. W. Clark, 2010. *NIST Handbook of Mathematical Functions*, 1st ed., Cambridge University Press, New York, NY, USA.

Opitom, C., E. Jehin, J. Manfroid, D. Hutsemékers, M. Gillon, and P. Magain, 2015. TRAPPIST monitoring of comet C/2012 F6 (Lemmon). A&A., 574, A38, doi: 10.1051/0004-6361/201424582.

Opitom, C., A. Guilbert-Lepoutre, E. Jehin, J. Manfroid, D. Hutsemekers, M. Gillon, P. Magain,G. Roberts-Borsani, and O. Witasse, 2016, Long-term activity and outburst of comet C/2013 A1 (Siding Spring) from narrow-band photometry and long-slit spectroscopy. A&A, in press

Press, W. H., B. P. Flannery, S. A. Teukolsky, and W. T. Vetterling, 1992. Numerical recipes in Fortran 77. The Art of Scientific Computing, 2 ed., Cambrige University Press, Cambridge.

Quémerais, E., J.-L. Bertaux, O. Korablev, E. Dimarellis, C. Cot, B. R. Sandell, and D. Fussen, 2006, Stellar occultations observed by SPICAM on Mars Express, J. Geophys. Res., 111, E09S04, doi:10.1029/2005JE002604

Rousselot, P., S. M. Hill, M. H. Burger, D. A. Brain, C. Laffont, and G. Moreels, 2000. Theoretical Modeling of the C 2 Fluorescence Spectrum in Comet Hale-Bopp. Icarus, 146, 263–269, doi: 10.1006/icar.2000.6383.

Rubin, M., V. M. Tenishev, M. R. Combi, K. C. Hansen, T. I. Gombosi, K. Altwegg, and H. Balsiger, 2011. Monte Carlo modeling of neutral gas and dust in the coma of Comet 1P/Halley. Icarus, 213, 655–677, doi: 10.1016/j.icarus.2011.04.006.

Savitzky, A., and M. J. E. Golay, 1964. Smoothing and differentiation of data by simplified least squares procedures. Anal. Chem., 36(8), 1627–1639, doi: 10.1021/ac60214a047.

Schleicher, D. G., 2010. The Fluorescence Efficiencies of the CN Violet Bands in Comets. Astron. J., 140, 973–984, doi: 10.1088/0004-6256/140/4/973.

Stiepen, A., L. Soret, J.-C. Gérard, C. Cox, and J.-L. Bertaux, 2012. The vertical distribution of the Venus NO nightglow: Limb profiles inversion and one-dimensional modeling, Icarus, 220, 981–989, doi: 10.1016/j.icarus.2012.06.029.

Tenishev, V., M.R. Combi and M. Rubin (2001), Numerical Simulation of Dust in a Cometary Coma: Application to Comet 67P/Churyumov-Gerasimenko, *Astrophys. J.*, 732: 104, doi: 10.1088/0004-637X/732/2/104

Tenishev, V., M. Combi and B. Davidsson (2008), A Global Kinetic Model for Cometary Comae: The Evolution of the Coma of the Rosetta Target Comet Churyumov-Gerasimenko throughout the Mission, *Astrophys. J.*, 685, 659, doi: 10.1086/590376.

Weiler, M., 2007. Study of the gas and dust activity of recent comets. Ph.D. thesis, Technische Universität Berlin, Berlin.

Weiler, M., 2012, The chemistry of C3 and C2 in cometary comae. I. Current models revisited, A&A, 538, id.A149, doi: 10.1051/0004-6361/201117480.

Figures and captions.

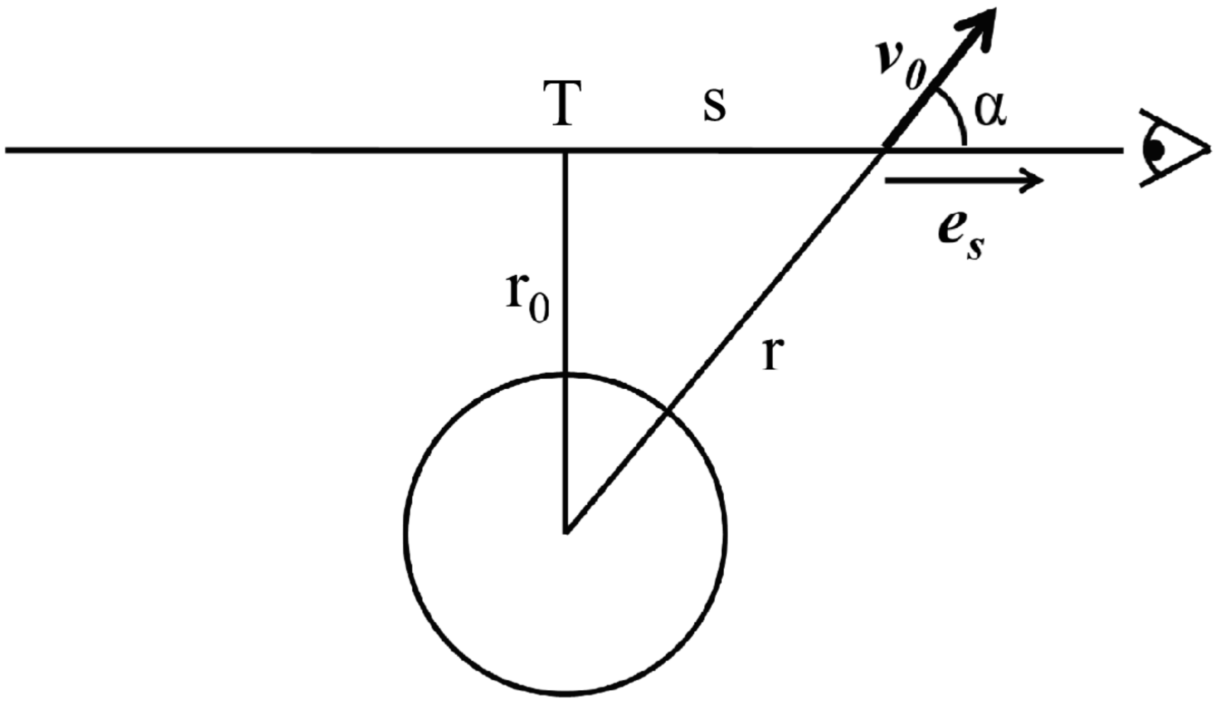

Figure 1. Geometry of the observation of an expanding coma. A remote observer collects the light emitted by the gas of the coma, summed up along the line of sight that passes through the tangent point T, i.e., the point of the line of sight nearest to the comet center. T is at a distance r_0 of the comet center, while a point of the line of sight is at distance r from the center. Variable s is counted from point T along the line of sight and can be considered to vary between $-\infty$ and $+\infty$ when the observer is at great distance. The coma expands radially at a velocity v_0. The angle between the expansion direction and the line of sight, noted α, changes along the line of sight.

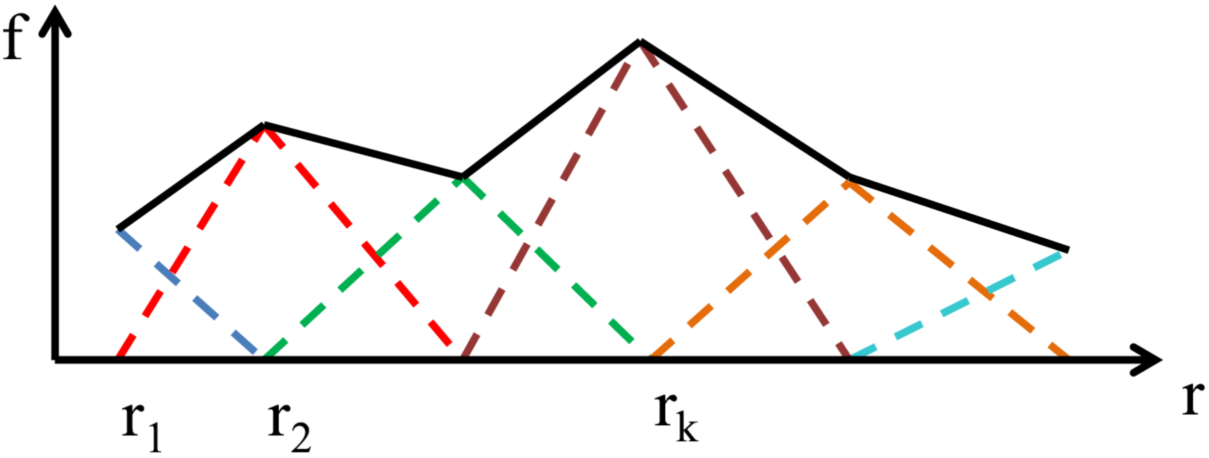

Figure 2. Representation of a function *f* decomposed into a set of linear segments using a linear combination of triangular functions. The sum of the colored dash lines triangles gives *f*, represented with the black segments.

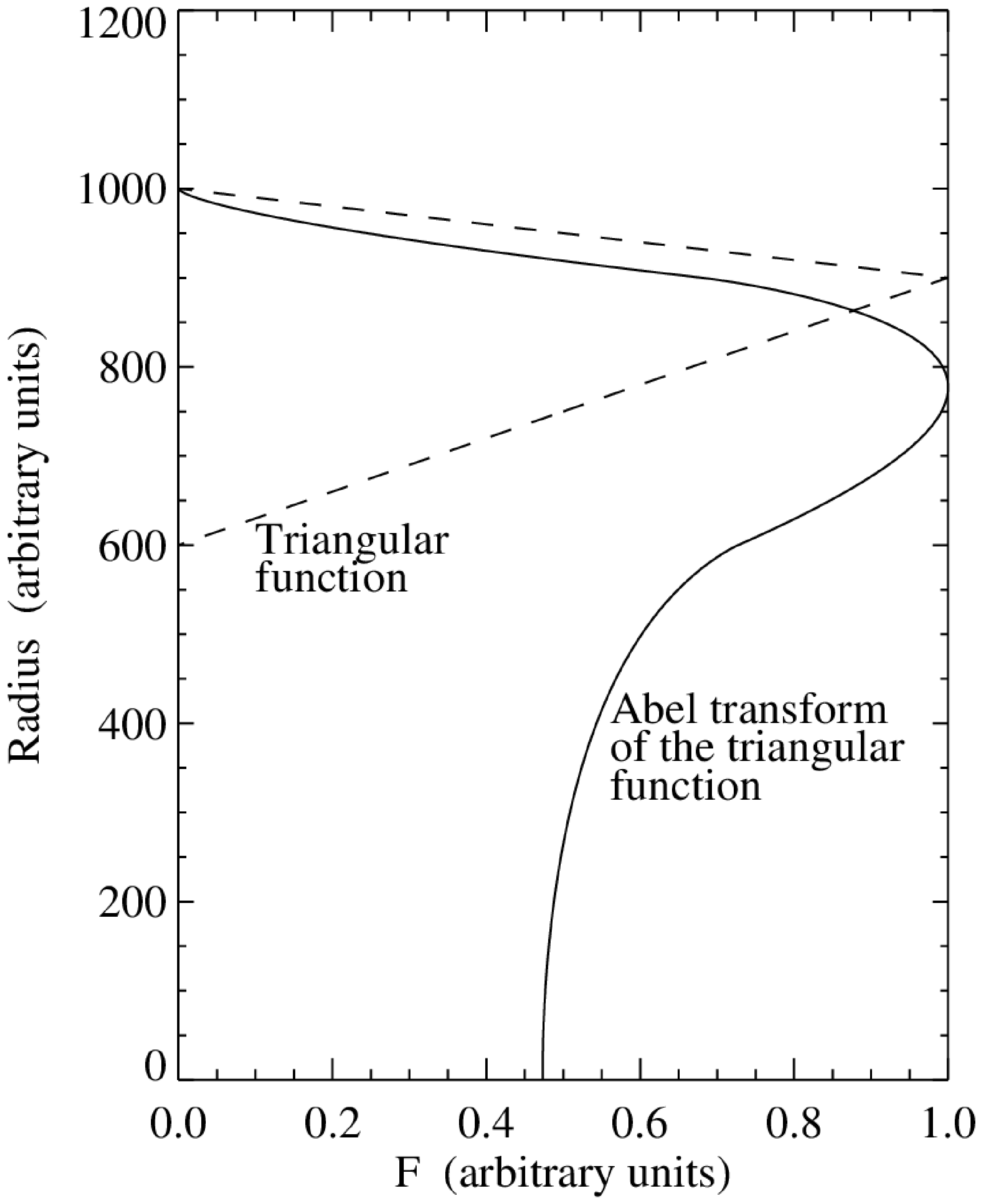

Figure 3. A triangular function and its Abel transform, both shown in arbitrary units. The peak of the Abel transform occurs at a somewhat lower radial distance than that of the summit of the triangle.

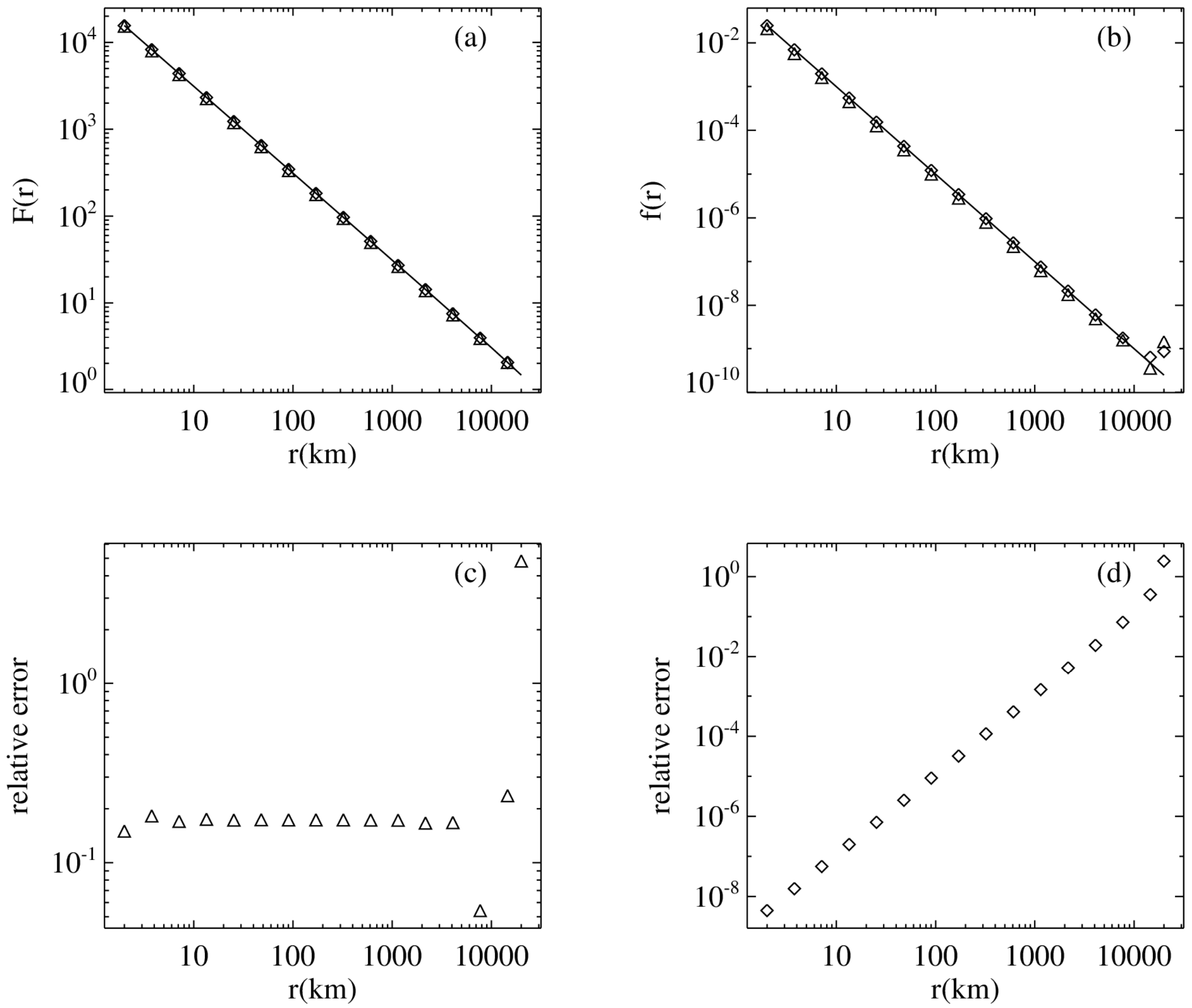

Figure 4. Abel transform of a theoretical nucleo-centric profile varying as $1/r^2$. Panel (a) shows the Abel transform F: the solid line gives the exact analytical values, triangles and diamonds show the profiles obtained after inverse transform fitting using purely triangular elements and triangular elements multiplied by $1/r^2$ respectively. Panel (b) shows the emission rate profile f, of which F is the Abel transform. Triangles show the emission rate profile fitted using triangular elements; diamonds represent the profile fitted using triangular elements multiplied by $1/r^2$. Panels (c) and (d) show the absolute value of the relative difference between the exact and the fitted emission rates obtained using the purely triangular elements and the triangular elements multiplied by $1/\mathrm{r}^2$, respectively. No regularization was applied for these inverse Abel transform fits.

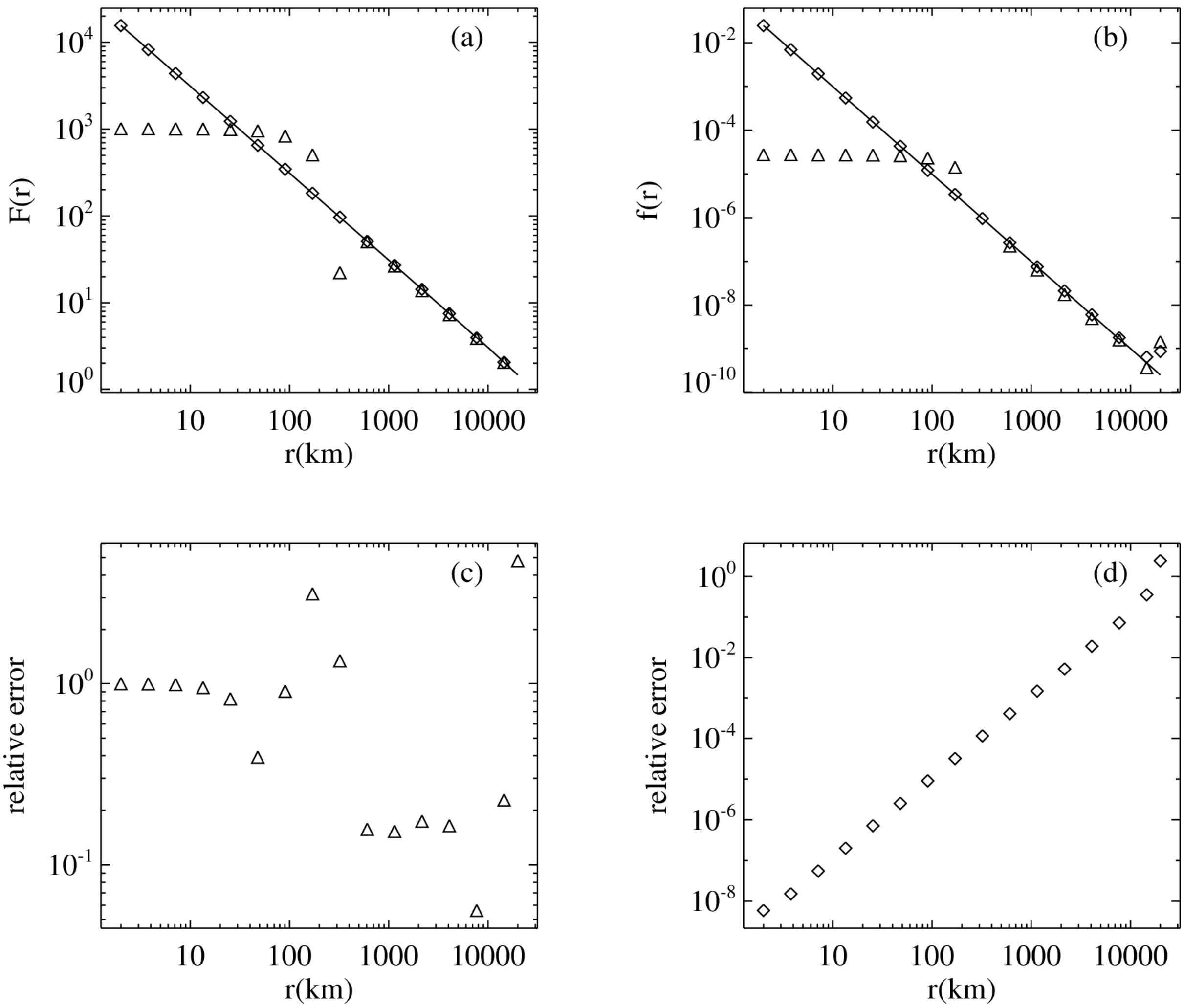

Figure 5. Same as figure 4, but combined with a Tikhonov regularization.

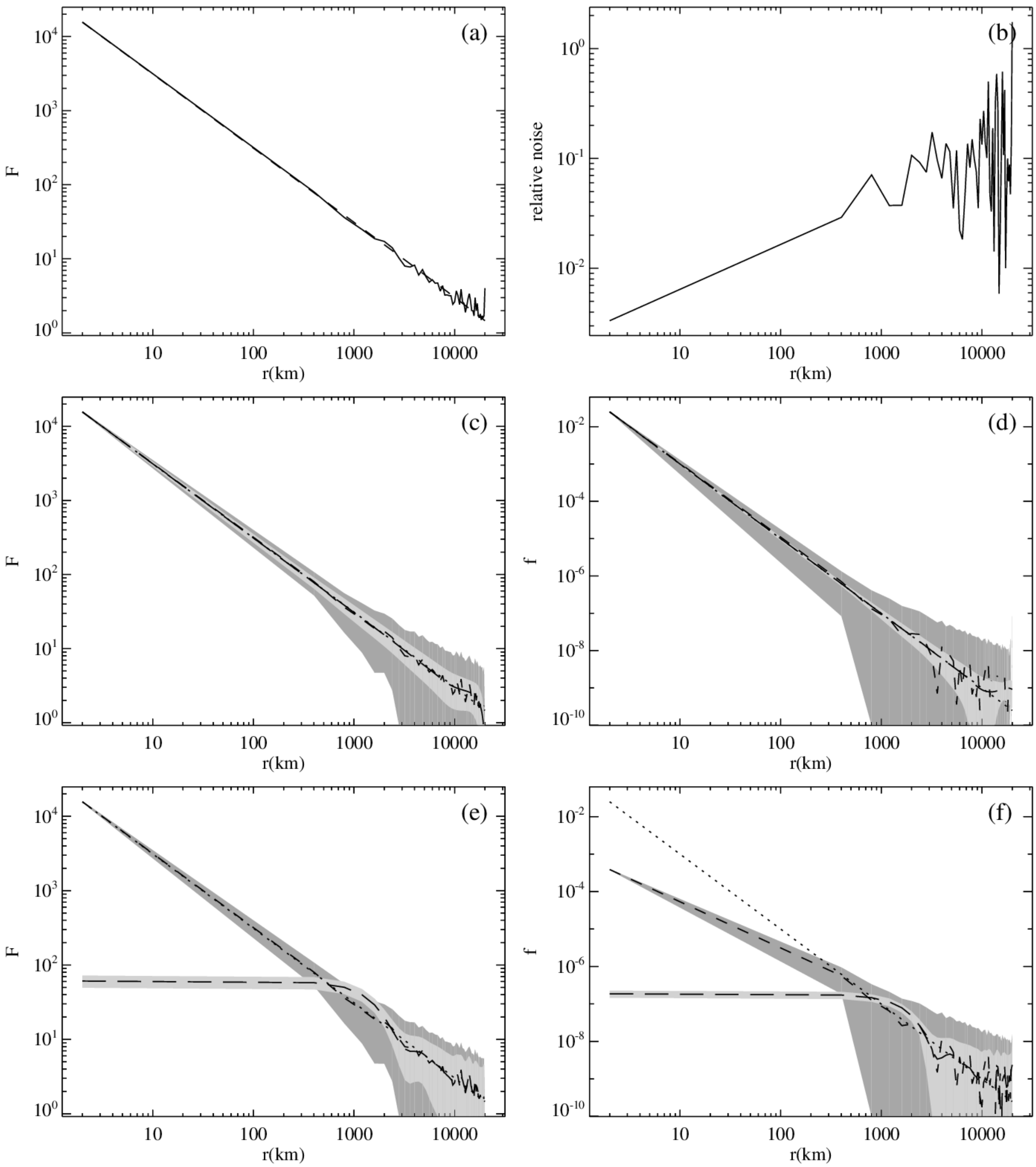

Figure 6. Inversion of a realistic simulated profile including noise and a regular binning. Panel (a): line-of-sight integrated profile, i.e., Abel transform of the ~$1/r^2$ emission rate. The dashed line shows the exact transform, while the solid line shows the noisy values to be used in the inverse Abel transform method. Panel (b) shows the absolute value of the relative difference between the noisy and the smooth profiles from panel (a). Panel (c) shows the exact Abel transform (dotted line) and the values fitted over the noisy profile of panel a, using triangular elements divided by r^2. Short (long) dashes show the fitted profile obtained without (respectively with) regularization. The dark (light) grey shade show the ±1σ interval obtained applying error propagation for the unregularized (respectively the regularized) fit. Panels (e) and (f) are similar to panels (c) and (d), respectively, using purely triangular elements for the fits instead of triangles divided by r^2.

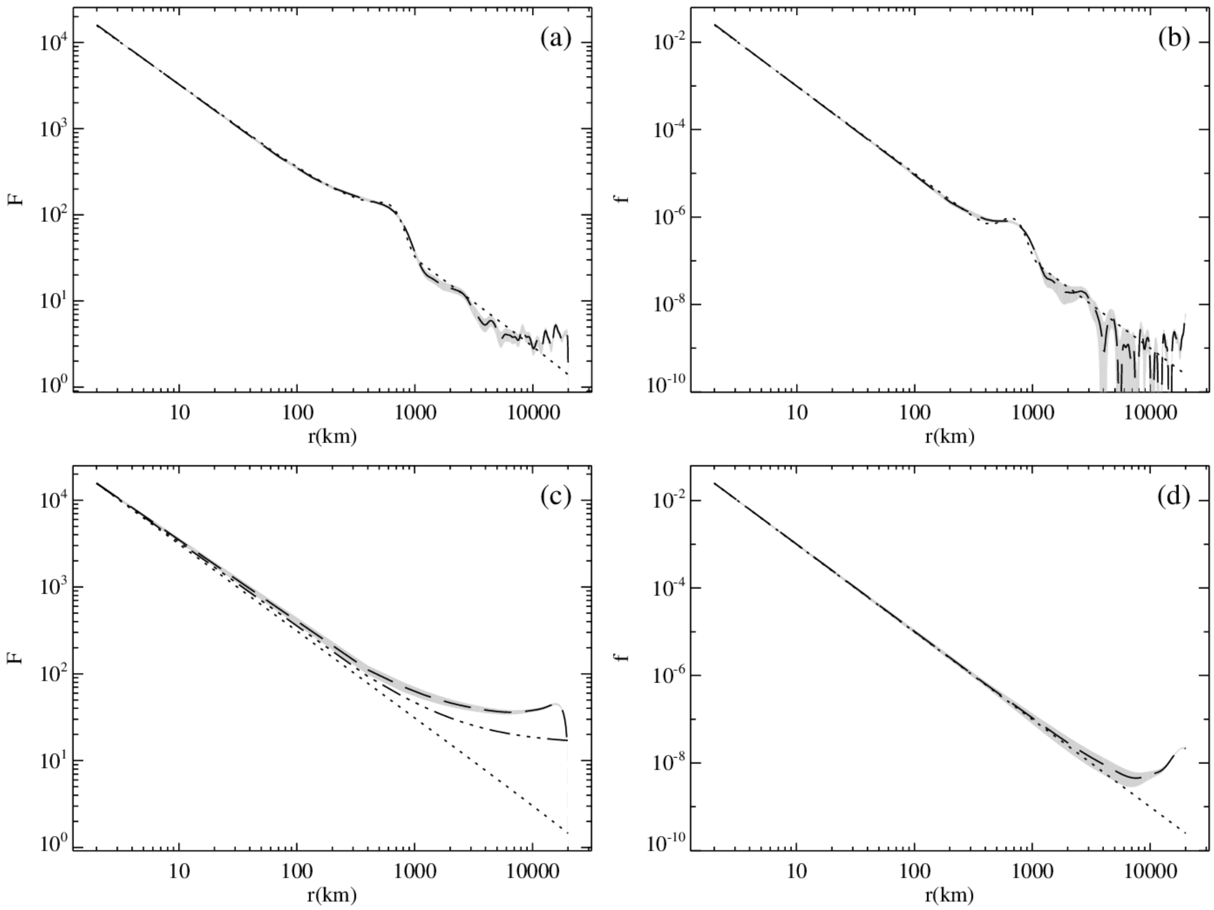

Figure 7. Inversion of a ~1/*r* l.o.s.-integrated profile modified by a Gaussian disturbance (panels (a) and (b)). The ideal disturbed l.o.s.- integrated profile is represented by the dotted line in panel (a). The noisy signal actually used as input for the inversion algorithm is omitted for clarity. The long dashes show the fitted l.o.s.-integrated profile, the grey shade delimits the 1–σ uncertainty band. Panel (b) shows the local emission rate, the dotted line represents the exact profile that we seek to retrieve; the long dashes show the fitted profile with the 1–σ uncertainty delimited by the grey shade. Panels (c) and (d) show the results from the inversion of a power law profile augmented by a constant offset. In panel (c), the dotted line shows the ~1/*r* l.o.s.-integrated profile, the dash-dot-dot-dot line shows the same profile increased by a constant amount while the long dashes show the fitted profile with the grey shade delimiting the ±1σ uncertainty band. Panel (d) shows the target ~1/r^2 emission rate profile, the long dashes represent the fitted profile and the grey shade delimits the ±1σ uncertainty band.

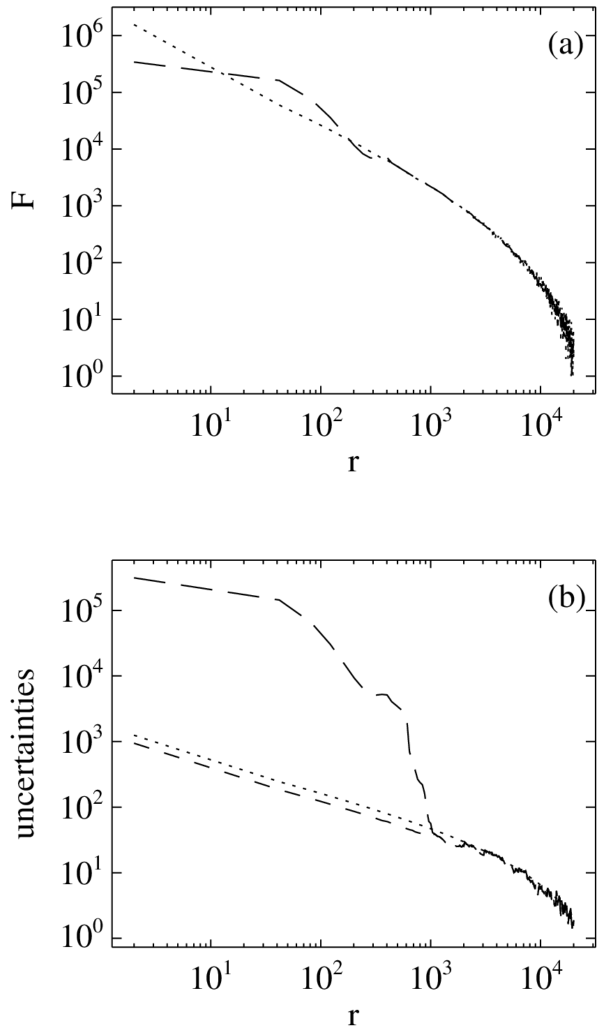

Figure 8. Panel (a): shows a simulated noisy l.o.s.-integrated Haser profile before (dotted line) and after smoothing with a Savitsky-Golay filter (long dashes). Panel (b) shows the standard deviation used to generated the noise of the profile shown in panel (a) (dotted line), which is just the square root of the ideal profile (i.e., before artificial noise contamination). The long dashed line shows the standard deviation estimated using the smoothed profile of panel (a) and applying the formulas of equation (37) , while the short dashes show the uncertainties obtained applying a square root scaling near the inner boundary of the profile.

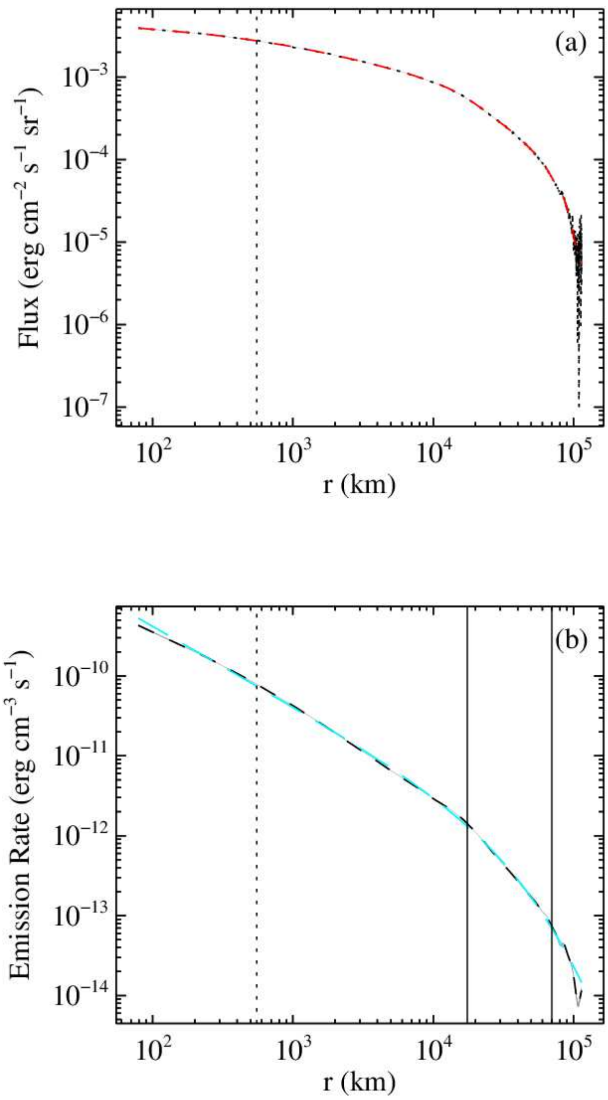

Figure 9. Observation of the CN emission of comet 103P/Hartley2 on 07 November 2010 at 387 nm. Panel (a) shows the observed flux, i.e., the l.o.s.-integrated data (dotted line). The red long dashed curve shows the fitted flux obtained with the inverse Abel transform method; uncertainties are shown as grey shades (they are lower than the line thickness in the plot). Panel (b) shows the emission rate obtained using the inverse Abel transform of the observed flux shown in panel (a) (black short dashes), with the uncertainties indicated by grey shades (which are again smaller than the line width in the plot). The blue long dashes show a Haser model fitted to the black dashes. It has characteristic lengths L_p= 17500 km and L_d= 70100 km, indicated by the vertical solid lines. The vertical dotted lines correspond to the fourth data point of the observation.

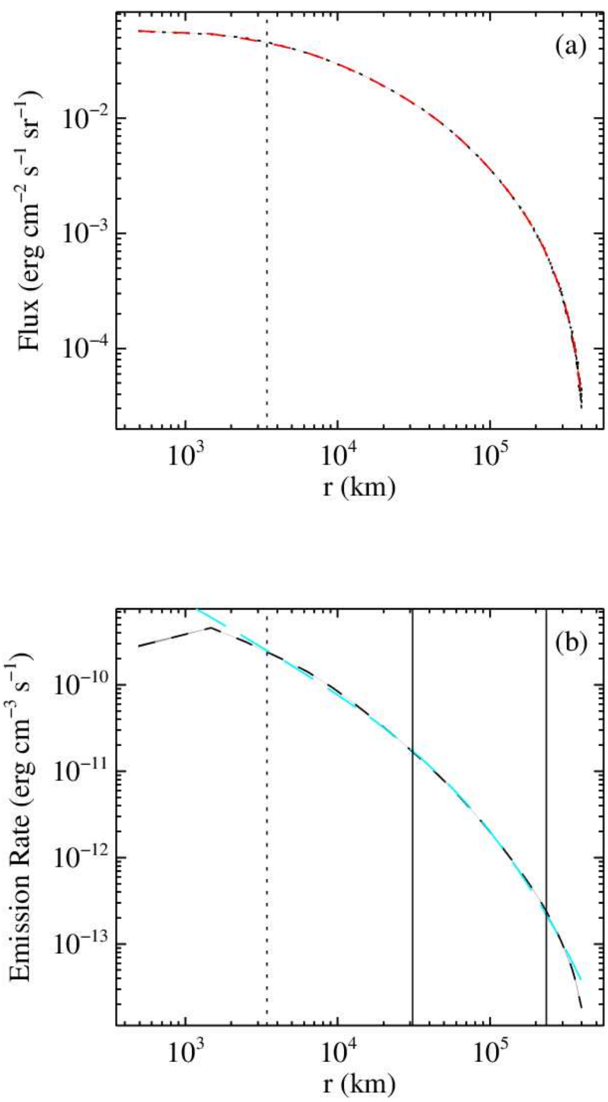

Figure 10. TRAPPIST observation of the CN emission at 387 nm of comet C2012 F6/Lemmon on February 17, 2013 (line styles and colors as in **Figure 9**). The characteristic lengths of the fitted Haser profile are L_p = 31100 km and L_d = 235000 km, indicated by the vertical solid lines. The vertical dotted lines correspond to the fourth data point of the observation.

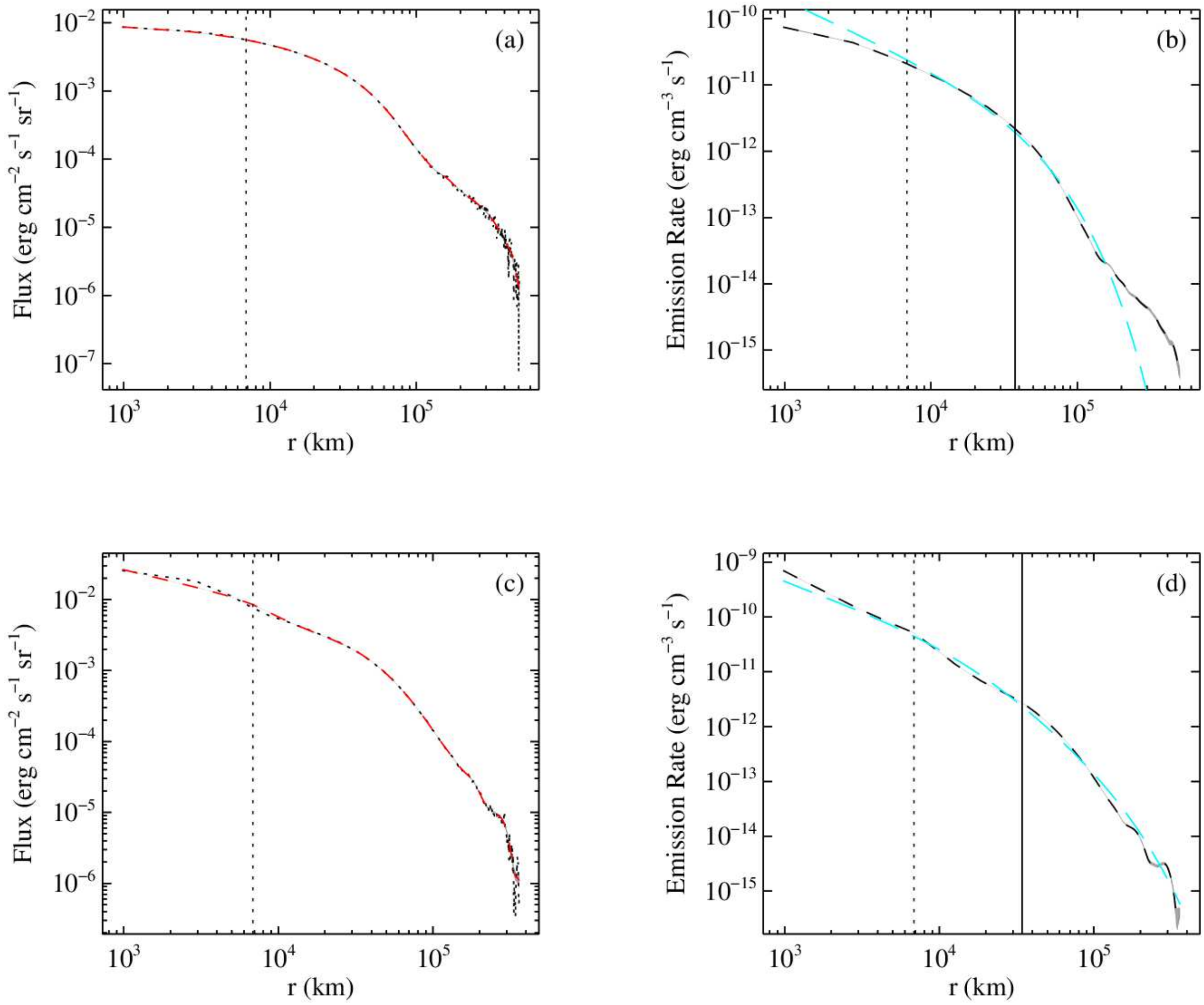

Figure 11. Radial profiles of the emissions of molecules CN at 387 nm (panels (a) and (b)) and C_2 at 514.1 nm (panels (c) and (d)) from comet C/2013 A1 Siding Spring on November, 11 2014. Line styles and colors are the same as in **Figure 9**. The characteristic lengths of the fitted Haser models are L_p = 37646 km and L_d = 37688 km for CN and L_p = 34273 km and L_d = 34302 km for C_2. The vertical dotted lines correspond to the fourth data point of the observation.

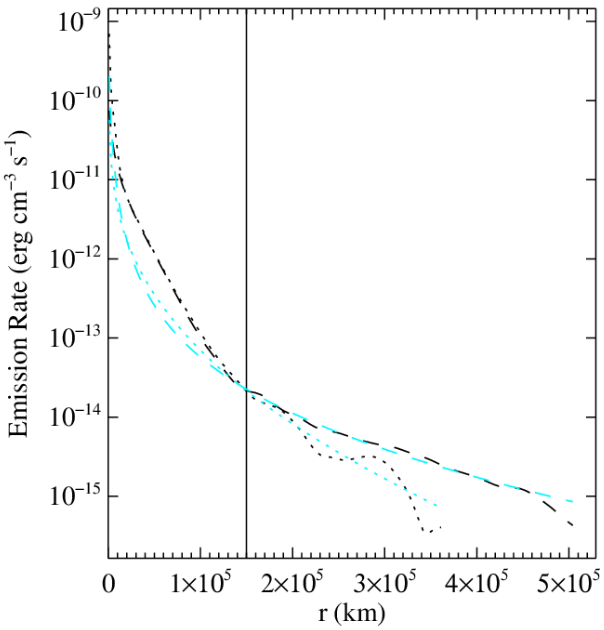

Figure 12. Radial profile of the emission rates of CN at 387 nm (black dashed line) and of C_2 at 514.1 nm (black dotted line) obtained by inverse Abel transform fitting of the ESO-TRAPPIST observation of comet C/2013 A1 Siding Spring on November, 11 2014. The light blue lines represent a Haser model fitted to the emission rate of CN (dashed line) and C_2 (dotted line) at nucleo-centric distance larger than 1.5×10^5 km. The vertical line indicates the breaking of both radial profiles as an outburst signature, separating the pre- and post-outburst gas.

	Q_{HCN}	$Q_{HCN}^{(F)}$
103P/ Hartley 2	2.684	3.22
F6/ Lemmon	88.8	102
A1/ Siding Spring	42	

Table 1. Production rates of HCN inferred by least squares fitting of the emission rate (Q_{HCN}) and observed flux ($Q_{HCN}^{(F)}$) profiles for comets Hartley 2, Lemmon and Siding Spring (in 10^{25} particles s^{-1}). This latter comet experienced an outburst so that the production rate obtained by the least squares fitting is of little significance and only Q_{HCN} is listed.